A Fully 3D Printed Waveguide and its Application as Microfluidically Controlled Waveguide Switch

by

Sabreen Khan

A thesis submitted in partial fulfillment of the requirements for the degree of

Master of Science
in
Electromagnetics and Microwaves

Department of Electrical and Computer Engineering
University of Alberta

Abstract

Hollow rectangular waveguides are employed extensively in microwave and millimeter wave devices owing to their relatively high power handling capabilities and low losses, particularly at higher frequencies, compared to transmission lines. However, the fabrication of such metal waveguides suffer from the challenge of needing expensive techniques and specialized labor, which is exacerbated as frequency increases into the millimeter- wave band, due to the increasingly demanding requirements in mechanical precision for smaller feature sizes, owing to the inverse relationship between wavelength and frequency. As a result, alternate techniques have been explored to make unit level manufacturing of waveguides, economical.

By the advancements of 3D-printing, also known as additive manufacturing (AM) technology, localized manufacturing of customized 3D structures offer the potential of abating the fabrication cost of such hollow rectangular waveguides for small to medium market size such as that of Satellite communication. As an emerging manufacturing alternative, 3D-printing has found widespread applications in rapid prototyping and manufacturing of high geometrical complexity components, over the years.

This thesis reports the design, fabrication and characterization of a waveguide fabricated with 3D-printing technology, and a microfluidically controlled waveguide switch, operating at K-band. The waveguide body is printed using a bench top 3D-

printer using thermoplastic substrate Acrylonitrile butadiene styrene (ABS), which gives the waveguide it's structure. In order to achieve functionality, the conductive part is realized by automated deposition of conductive silver ink to coat the waveguide walls. The fabricated waveguide is characterized exhibiting a total measured insertion loss of better than 0.11 dB/cm for the entire K-band. Its attenuation and propagation constants are computed for the K-Band using a multi-line technique. The results show reasonable agreement with simulations depicting 3D-printing followed by ink dispensing as an alternative waveguide manufacturing technology.

Additionally, a microfluidically controlled Eutectic Gallium Indium (EGaIn) liquid metal is integrated with the 3D-printed waveguide and a novel reflective waveguide switch is implemented. The measured S-Parameters are in accord with simulations, exhibiting ON State insertion loss and OFF State isolation to be better than 0.5 dB and better than 15 dB for the entire K-Band, respectively. Furthermore, the switch's performance with respect to changes in ambient temperature has been studied and was found fairly consistent.

To our knowledge, this is the first time that fully 3D-printed waveguide has been investigated wholly using a desktop 3D printer, with thermoplastic and conductive silver ink. In addition, this thesis reports the development of a novel microfluidically controlled reflective waveguide switch, which is incorporated into the reported 3D printed waveguide as well as conventional rectangular waveguides, exhibiting the potential of such technology for rapid prototyping of functional RF devices.

To enhance the performance of the ink coated 3D printed waveguides, the ink coated 3D printed waveguides was plated with copper and it is fully characterized. Additionally, this technique was also applied for the fabrication of a Single-Pole Double Throw switch to demonstrate the microfluidic concept further.

Preface

Chapter 3 and 4 of this thesis has been 'accepted for publication -- pending satisfactory resolution of reviewer comments' on August 24th 2016, as Sabreen Khan, Nahid Vahabisani, and Mojgan Daneshmand "A Fully 3D Printed Waveguide and its Application as Microfluidically Controlled Waveguide Switch", IEEE Transactions on Components, Packaging and Manufacturing technology. I was the lead investigator, responsible for all major areas of concept formation, fabrication, measurements and analysis, as well as manuscript composition. Nahid Vahabisani assisted in measurements and contributed to manuscript edits. Dr. Mojgan Daneshmand was the supervisory author on this project and was involved throughout the project in concept formation and manuscript composition.

A version of Appendix A has been submitted for publication as Nahid Vahabisani, Sabreen Khan, and Mojgan Daneshmand "A K-Band Reflective Waveguide Switch Using Liquid Metal", in IEEE Antennas and Wireless Propagation Letters, and is used with permission. A portion of this submitted manuscript has been re-printed in Section 4.4.3. I was responsible for implementing the liquid metal control setup and switching speed calculations. Appendix B has been directly adapted from the Ph.D. Thesis by Nahid Vahabisani, titled "3D Micro-fabricated Millimeter-wave Devices: Waveguides and Waveguide Switches," University of Alberta, Canada, 2014, with permission from author.

In Chapter 2, Fig. 2-1 is used with permission from applicable sources.

Acknowledgments

This thesis owes its existence to several people for their help, support and inspiration. Firstly, I would like to express my most sincere gratitude to my supervisor, Dr. Mojgan Daneshmand, for her continuous support, guidance, patience and suggestions throughout my research under her direct supervision. I consider myself very fortunate for being able to work with such a considerate and encouraging professor like her.

I would also like to thank my committee members, Dr. Douglas Barlage and Dr. Hyun-Joong Chung, for their time and efforts in the process and for their insightful comments and suggestions. Additionally, I would like to thank CMC Microsystems Canada, Natural Sciences and Engineering Research Council of Canada (NSERC), and the Canada Research Chairs (CRC) Program and MDA for funding support. I would like to acknowledge MDA for their support and suggestions.

My sincere thanks goes to my colleagues at the Microwave to Millimetre-wave Micro/Nano Technology (M2M MNT) Lab for the all their support, constructive suggestions and thought-provoking discussions. I would like to extend my gratitude particularly to an inspiring person, my colleague Nahid Vahabisani. Without her unconditional assistance and encouraging support, completion of this thesis would not have been possible. Very special thanks also go to my colleague Thomas Jones for his unhesitant help with electroplating and surface profiling. Also, thanks to Sameir Deif for his help with electroplating. Despite their busy schedules, the support they provided me has been phenomenal.

Thanks to all faculty and staff of the Electrical and Computer Engineering Department at University of Alberta for the enriching classes I took here during my studies.

It goes without saying that I would not have been here if it weren't for the remarkable support of my family. Finally, I must express my very profound gratitude to my husband, Hasan Rahman, for providing me with unfailing support and relentless encouragement through telephone chats, throughout the extremely stressful two years of my studies.

Table of Contents

List of Abbreviations

Additive manufacturing (AM)

Computer Aided Design (CAD)

Stereolithography (SLA)

Liquid thermal polymerization (LTP)

Beam interference solidification (BIS)

Solidification of an electroset fluid: Electrosetting (ES)

Ballistic particle manufacture (BPM)

Fused deposition modelling (FDM)

Three dimensional welding (3DW)

Shape deposition manufacturing (SDM)

Selective laser sintering (SLS)

Gas phase deposition (GPD)

Three dimensional printing (3DP)

Spatial forming (SF)

Sheets bonded with adhesive: laminated object manufacture (LOM)

Sheets bonded with UV light: solid foil polymerisation (SFP)

Acrylonitrile butadiene styrene (ABS)

Eutectic Gallium Indium (EGaIn)

List of Figures

1 Introduction

1.1 Motivation

Hollow metal waveguides hold substantial importance in the RF world, due to their excellent RF performance at microwave and millimeter frequencies, compared to conventional planar transmission lines. This technology is essential for applications where dissipative attenuation is a crucial factor. As the result, waveguides and their applications as waveguide switches have been extensively used for the majority of high-frequency low-loss applications since decades. Conventionally, waveguide fabrication involves extensive micromachining that involves metal-working processes, for instance, milling, drilling, lathing, shaping, brazing, Electron Discharge Machining, and other associated process demanding heavy machinery and trained professionals.

The advent of 3D printing, also known as Digital Additive Manufacturing (DAM), has seen a proliferation of fabrication techniques for 3D structures. It has gained recent popularity among researchers as a promising fabrication alternative.
The governing fundamentals and working principle of 3D printing offer a spectrum of advantages. To begin with, 3D printing allows customizing complex designs easily without the need for changing the tool and at no additional production cost. In addition, for low quantity production markets such as that of satellite industry, it is expected to cost significantly lower that existing moulding manufacturing techniques. Contrary to the traditional subtractive machining and lithographic techniques, additive manufacturing is an energy efficient technique with less waste material. A promising feature of the 3D printing technology is its 'local on-demand' manufacturing ability, abating the need for massive inventories and unsustainable logistics for shipping high volumes of products around the world. Notable use of this is in the defence and space applications, where these issues are of primary importance.

Owing to the fabrication challenges of using conventional fabrication technology for waveguide manufacturing, this thesis aims to explore to possibilities of using 3D printing as an alternative. This thesis also inclines to explore the possibilities of integrating liquid metal in microfluidic channels to simplify the fabrication of a reflective waveguide switch. These techniques are motived to eliminate the complicacy in RF electronics fabrication.

1.2 Objective

The core incentive of this thesis is to study high frequency RF devices with additive manufacturing. Owing to the advantages of 3D printing and the importance of hollow waveguides stated above, this thesis aims to utilize the fabrication technology and apply it for the manufacture of waveguide and waveguide devices that are imperative to the RF world. This work is anticipated to exhibit how additive manufacturing technology has evolved to include greater functionality and embrace a wider range of applications beyond the initial intention of just prototyping.

The foremost goal of this thesis is to explore the potential of 3D printing as an alternative manufacturing technology for fabricating a hollow rectangular waveguide. To achieve this goal, a commercially available bench-top 3D printer (X-series, Machina Corp), retrofitted with ink printing capabilities was used with thermoplastic and silver conductive ink as raw materials. The designed waveguide model will be fabricated and characterized for the operating K-band. This thesis also investigates the possibility of using waveguide electroplating by using ink as adhesive material for improved RF performance. Attempts at improving the performance of the device, alternative metallization technique will also be experimented. This thesis also investigates the possibility of using waveguide electroplating by using ink as adhesive material for improved RF performance.

Subsequently, the application of the 3D printed waveguide as a microfluidically controlled waveguide switch will be investigated. To achieve this aim, the fundamental step will be to design, model and optimize the conceptual fluidic switch. To further demonstrate its potential, the switch concept will be extended to a Single-

Pole Double-Throw microfluidically controlled waveguide Switch application fabricated through 3D printing.

1.3 Thesis Outline

This thesis is divided into five chapters. A brief introduction to the motivation and objective of the work is presented in Chapter 1. Chapter 2 compiles a review of existing 3D printing technologies and applications, in addition to a background of waveguides and addresses their fabrication challenges, followed by comprehensive literature review of waveguide switches. This chapter additionally outlines previous works that utilizes microfluidic tuning. Chapter 3 presents the design, fabrication and RF characterization of a K-Band hollow rectangular waveguide, fabricated using 3D printing technology, using thermoplastic and conductive ink. In Chapter 4, an application of the 3D printed waveguide as a microfluidically controlled reflective waveguide switch is developed and detailed in terms of design concept and RF performance. Chapter 5 compares the performance of ink coated 3D printed waveguides with the metallization technique: Electroplating. Additionally, the microfluidically controlled switch concept developed in Chapter 4 is extended to develop a Single-Pole Double-Throw (SPDT) switch, measurements of which are exhibited in this Chapter 5. Chapter 6 summarizes the conclusions of this thesis and outlines the scope for further research.

2 Review of Literature

2.1 3D-Printing Overview

3D printing is a process for making a 3-D physical object from a 3-D digital model, using layer-by-layer selective addition of successive thin layers of material. 3D printing, also known as Additive manufacturing (AM), made its entrance in the late 1980's [1], and today, it has gained enormous popularity among researchers as a promising rapid prototyping fabrication alternative.

2.1.1 Advantages of 3D Printing

Additive Manufacturing (AM), also common called 3D printing, offers several advantages over traditional subtractive manufacturing techniques. To begin with, 3D printing allows the personalized customization according to end-user requirements. It has also made a significant impact on industrial applications, whereby applications are being developed to materialize complex components that are proving to be both lighter and stronger than their predecessors. In traditional manufacturing, complexity in design increases the manufacturing cost. With additive manufacturing, the time, effort and cost to create complex designs are comparatively lower, making it possible to produce highly optimized products without being bogged down by manufacturing cost. Thus, products and components can be designed specifically to avoid assembly requirements with intricate geometry and complex features.

For decades, there has been significant hurdle for new product introductions in the industry, requiring the product to undergo numerous transformations till a final optimized product is achieved. Generally, the cost involved in prototyping a new design and model, is enormous. Using 3D printing for rapid prototyping allows manufacturers to circumvent the lengthy process of conventional prototyping by modeling and printing a scaled-down or full-scale replica of the designed product for

quick availability and testing. For industrial manufacturing purposes, one of the most costly, time consuming and labor intensive stages of the product development process is the production of individual tool for each structural design. This allows design teams to test the prototype at an early stage and make any necessary modifications to the design before any commitment to production tooling is made. Without the need for a change in tool, 3D printing leads to reduction of costs, leads times and associated labor for rapid prototyping of new products. Moreover, since a 3D printer can print on demand, it reduces the need for companies to stockpile physical inventory.

Furthermore, conventional manufacturing process are subtractive in nature, where a mass of material is modified by removing (subtracting) parts of the material to achieve the designed final geometry. With metals, 3D printing generates less waste in comparison with traditional grinding or milling techniques used in conventional mass manufacturing. Machining metal is highly wasteful; an estimated 90 percent of the material ends up on the factory floor [2]. On the contrary, additive manufacturing process involves built-up of the designed CAD model, layer by layer. Thus, the process provides environment efficiencies in terms of maximum usage of raw materials, generation of less waste and subsequently imposing a reduced carbon footprint.

2.1.2 3D Printing Technologies

3D printing can be classified either according to the baseline technology for material creation or solidification, or on the basis of the shape building technique [3]. All the processes require the design of the geometry to be printed in the form of a 3D CAD model, which is sliced into layers and sent to the 3D printing machine for production. Fig. 2-1, re-printed from [4] adapted from [3], depicts the categorization of Rapid prototyping techniques into additive and subtractive technologies, where the AM technologies are further classified elaborately based on material creation technique. The additive manufacturing process is classified here based on the type of raw material used at input, i.e. liquid based technique, powder/ discreet particle based

technique and solid based technique. The work presenting in this thesis used FDM technology and its place in the Fig. 2-1 is marked as a point by point printing technique that prints by solidification of molten materials.

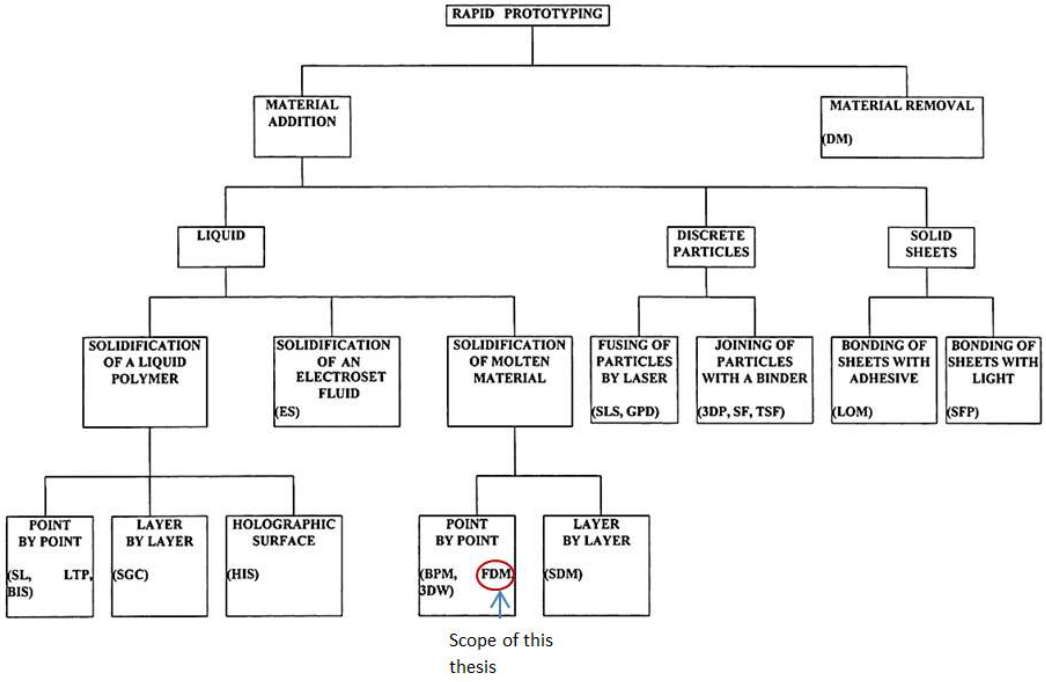

Fig. 2-1 Classification of rapid prototyping process (©1988 IJMTN, re-printed from [4], adapted from [3]).

2.1.3 3D Printed RF Electronics

Over the years, 3D printing, used as a rapid prototyping technique, have garnered tremendous popularity for the fabrication of not only conceptual models, but also fully functional prototypes [5]. The commencement of 3D printing mainly involved the use of non-conductive materials to print prototypes. Owing to the on-going advancements in the area of 3D printing, a wide range of materials can now be used for different 3D printing technologies. The 3D printing technology can be divided into two broad groups - Metallic and Non-metallic [6].

An example of the metallic 3D printing technology is Direct Metal Laser Sintering (DMLS) which is reported to fabricate waveguide planar antenna array made of aluminium metal alloy[7]. Recent interest in the metallic technique has also resulted in a series work involving Selective laser melting (SLM) using Cu-15Sn alloy powder, to fabricate conical horn antennas[6] [8], rectangular waveguides for mm-wave applications [9], and E-Band iris band-pass filters with waveguide interface[10]. Reports for the use of binder jetting to fabricate meshed rectangular Ku-band waveguide [11], and horn antenna [6] have also been reviewed.

However, the metallic 3D printing technologies require expensive and specialized printers, materials and experienced machine users for operation of the machines.

Some example of the non-metallic 3D printing technology include Stereolithography 3D printing technology used to fabricate 60-GHz integrated lens antennas [12] and 3D folded loop frequency selective surfaces (FSS) followed by manual application of silver paint coating [13]. Another commonly used non-metallic technique is Polymer-jetting 3D printing technology which has been reportedly used for fabrication of dielectric reflect-array antennas at THz frequencies [14], and low-gain Luneburg lens [15].

For the RF front end, the non-metallic 3D printing technique generally needs to be accompanied by a metallization process in order to make a non-metal structure to function as an EM component, e.g. coating with conductive aerosol paint [16].

The advent of conductive polymers has recently enabled the FDM process alone to print fully functional devices, using a conductive polymer [17]. Although it reduces the need for the additional metallization technique, such devices suffer from the drawback of low performance owing to low conductivity of the polymer used as feed material.

Printed RF Electronics with FDM:

Being on par with the scope of the thesis, an overview of functional electronics fabricated using the Fused Deposition Modelling 3D (FDM) printing technology followed by a metallization technique is presented below:

The FDM approach generally uses polymers Acrylonitrile Butadiene Styrene (ABS) and Polylactic acid (PLA)) as raw materials for the built. The dominantly reported 3D printed RF devices using FDM are printed with non-conducting polymers and thermoplastics like acrylonitrile butadiene styrene (ABS). To achieve a fully functional prototype of a device, the 3D printing technology needs to be incorporated with a metallization technique. Succeeding the polymer printing process, in order to gain the ability of having conduction currents, a conductive metal coating is required. A number of approaches have been reported for the metallization process.

The dominantly reported technique is automated dispensing of conductive ink on the non-conductive 3D printed structure. Fig. 2-2 illustrates examples of such work on the RF front End. Other examples are meander line 3D dipole antenna operating around 1GHz [18] as shown in Fig. 2-2 (a) and a 5 GHz conical spiral antenna [19]. Both the works used PLA substrate along with a combination of IIMAK conductive ink dispensed on the substrate to create the conductive meander lines.

The ink dispensing technique also enables conformal printing on curvilinear surfaces. Examples include a 1.7 GHz antenna 3D printed with FDM on a curvilinear laminate surface [20]. Another example is the dual- band dome antenna operating at 520 MHz and 710 MHz printed on hemispherical ABS substrate [21] with grooves indented. The groves were filled with conductive silver epoxy and polished Fig. 2-2 (b). [22] reports the fabrication of origami antennas operating at 2.4GHz for multi-direction RF Harvesting. An FDM 3D printer is used to print square slabs with hinges that soften when heated and allow the structure to fold in ‘origami’ style to a cuboid shape as shown in Fig. 2-2 (c). Patch antennas are printed on the slabs with silver nano-particle ink using an inkjet printer. A 2.45 GHz RF front end devices such as an open loop resonator, a circularly polarized dipole antenna, Fig. 2-2 (d,e) and a switched line phase shifter has been reported in [23]. The printing process integrates

FDM printing of ABS substrate, and micro-dispensing of silver conductive paste. Another example of such work is the fabrication of Microstrip line resonators for 4.7T MRI systems as reported in [24]. The material used in this work is ABS and PLA printed with a desktop printer retrofitted to dispense silver conductive ink on the printed structure.

One of the metallization technique involves spraying with a conductive aerosol paint [16], which suffers from the drawback of being less conductive and costly. Another metallization technique reported is plate a layer of metal over the 3D printed polymer structure, using electroplating and electroless plating processes [25]–[29]. An alternatively reported technique for metallization is ultrasonic wire mesh embedding technique which works as good as regular metal sheet at microwave frequencies. This technique has been reported to have been used for the fabrication of microwave patch antenna [30] and multilayer microstrip line structure [31]. The conductivity of the ink used plays a significant role in the performance of devices when metallization is realized with conductive ink coatings.

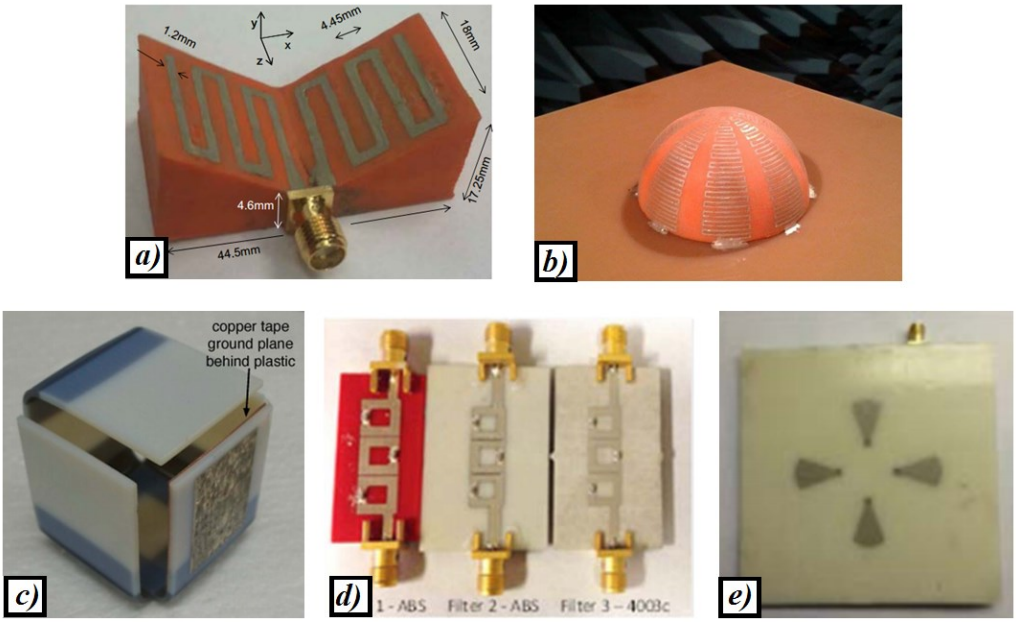

Fig. 2-2 3D printed devices metallized with conductive ink (a) meander line dipole antenna [18] © [2013] IEEE (b) dome antenna on a hemispherical substrate [21] © [2014] IEEE (c) Origami patch antenna [22] © [2015] IEEE (d) Band pass filters & (e) Crossed bow-tie dipole antenna [23] © [2015] IEEE.

An advantage of 3D printing fabrication technology is that it's a low-cost user-friendly and eco-friendly fabrication technology with short turn-around time. 3D printing metallic parts involves the use of expensive machinery, specialized, and experienced machine operators. On the other hand, 3D printing using FDM technology is a cheaper and highly commercial option/ FDM 3D printers are readily available, and user-friendly. Additionally the final product being majorly made of dielectric, with only a layer of metal coating, tend to make the devices light weight. According to [32], "The process of printing conductive paste and dielectric in one process is termed 'full 3D printing'". Hence the combination of FDM and Ink dispensing can be termed as a full 3D printing technology, eliminating the need for additional processes as reported in the literature. Therefore, this work investigates the possibilities of full 3D printing in RF applications.

2.2 Waveguide Background

Waveguides were of the earliest types of transmission lines used for the transmission of microwave signals, and are still routinely used to transfer large amounts of microwave power [33]. More recently, it has attracted lots of attention due to its superior performance at millimeter-waves. Driven by its use in the defence, aerospace, marine, communications industries and precision test applications, the waveguide technology is continuously evolving. Despite the fact that waveguides may assume any arbitrary but uniform cross section, common waveguides are either rectangular or circular, with rectangular waveguides being more widely used. Although the trend of miniaturization and integration has led to recent microwave devices to be fabricated on a planar platform, such as microstrip lines or striplines, at microwave frequencies (roughly 3-300GHz), these two conductor transmission lines become inefficient due to excessive conductor and dielectric losses. Hollow waveguides on the other hand, are a single conductor transmission line, in which the propagating electromagnetic fields are completely shielded, providing excellent isolation between adjacent signals. Additionally, with hollow rectangular waveguides,

there are no concerns regarding the spacing between or with the consistency of the dielectric material, since the only dielectric in a waveguide is homogeneous air. Consequently, waveguides are still widely used to obtain larger bandwidth and low-loss transmission of power at Microwave and Millimeter-wave frequencies. Moreover, contrary to transmission lines, a waveguide allows propagation only above its cut-off frequency, and therefore acts like a high-pass filter, enabling propagation of TM and TE modes only.

A diverse collection of waveguide components are available commercially for various standard waveguide bands. These include circulators, switches, couplers, detectors, isolators, attenuators, loads, filters, mixers, amplifiers and slotted lines. In fact, several waveguide sections, switches, twists, bends etc. that couple to the respective device, are often screwed together with flanges and adaptors to form an interconnected network. Fig. 2-3(a) shows some examples of waveguide components commercially available for standard waveguides. Such waveguides and waveguide components are deployed in industries, usually in the form of waveguide network, and are typically used to interconnect transmitters and receivers with antennas, such as the waveguide network in air traffic control radar shown in Fig. 2-3(b) [34].

However, these are only standardized components. For applications such as satellite and communication industries, new designs are daily generated to satisfy the even increasing demand of the new communication and wireless applications [35]. When the consumer market has low quantities, using traditional manufacturing technologies for developing such structures becomes very expensive. 3D printing could be a good alternative owing to its additive layer by layer manufacturing process.

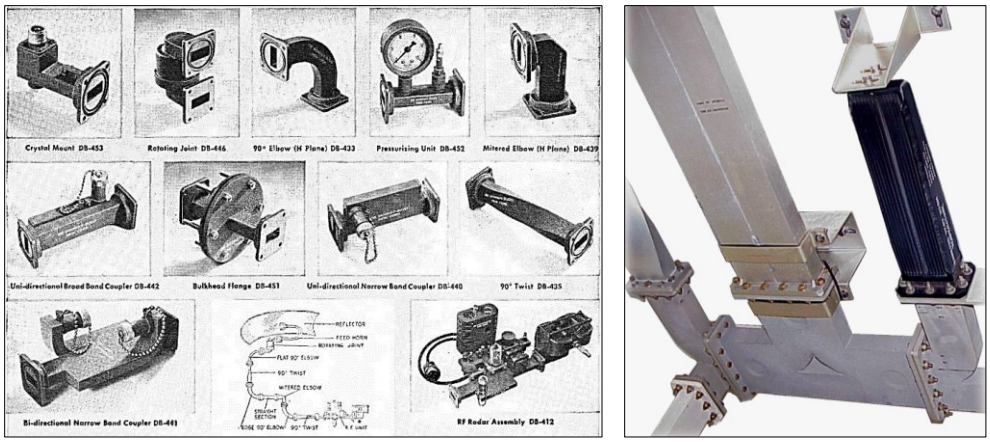

(a) (b)

Fig. 2-3(a) Collection of Standard waveguide components [36] (b) Example of a waveguides and a diplexer in air traffic control radar [34].

2.2.1 Metallic Rectangular Waveguide Theory

The geometry of a waveguide depicts its transmission properties. Fig. 2-4 shows a hollow rectangular waveguide in a rectangular coordinate system, filled with a material of permittivity ϵ and permeability μ, where a and b are the wider and narrower inner dimension respectively. The rectangular waveguide is a one-conductor propagating transmission line which only allows the propagation of Transverse Magnetic (TM) and/or Transverse Electric (TE) modes, characterized by the presence of longitudinal magnetic and electric field components, respectively [33]. Contrarily, TEM waves can only exist when two or more conductors are present, and hence, a closed conductor waveguide is unable to support TEM waves due to the boundary conditions.

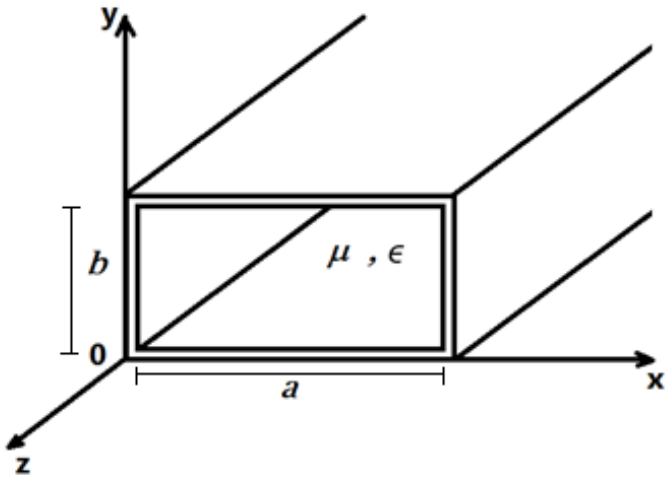

Fig. 2-4 Cross section of a waveguide with long dimension *a* and short dimension *b*.

Transmission modes are solutions of Maxwell's equations resulting from the boundary conditions imposed on the wave. Generally, all higher order modes have distinct cutoff frequencies and propagation takes place just above their cutoff frequencies. Subsequently, only a certain number of modes can propagate in a particular transmission line, each having a different field configuration. The TE modes have atleast one component in the direction of propagation, with all electric fields transverse to the axis. On the contrary, the TM modes are such that some electric field exists in the direction of propagation while all magnetic field components are transverse to the axis [37].

The propagating mode with the lowest cutoff frequency in a waveguide is called the dominant mode. Hence, propagation only takes place above the cutoff frequency all higher frequencies propagate within the waveguide. Thus, the cutoff frequency defines the high-pass filter characteristic of the waveguide: above this frequency, the waveguide passes power, below this frequency the waveguide blocks power.

Each mode of propagation can be represented by a combination of mode indices m and n. Applying the boundary conditions on the transverse field components of the TE_{mn} and TM_{mn} modes, and considering a lossless waveguides

($(\sigma = 0, \sigma_c \simeq \infty)$ with no attenuation (α= 0, γ=jβ), the propagation constant can be defined as:

$$\beta = \sqrt{k^2 - k_c^2} = \sqrt{k^2 \ - \left(\frac{m\pi^2}{a}\right) - \left(\frac{n\pi^2}{b}\right)} \tag{2-1}$$

Where k is the wavenumber of the material filling the waveguide region, represented as

$$k = \omega\sqrt{\mu\epsilon} = 2\pi f \sqrt{\mu\epsilon} \quad (1/\mathrm{m}) \tag{2-2}$$

and k_c, is the cutoff wavenumber for a rectangular waveguide.

At a given operating frequency, the propagation constant needs to be real for propagation of fields in the mode. This happens when

$$k > k_c = \sqrt{\left(\frac{m\pi^2}{a}\right) + \left(\frac{n\pi^2}{b}\right)} \tag{2-3}$$

As a result, each mode has a cutoff frequency $f_{c_{mn}}$ and cutoff wavelength λ_c

$$f_{c_{mn}} = \frac{k_c}{2\pi\sqrt{\mu\epsilon}} = \frac{1}{2\pi\sqrt{\mu\epsilon}}\sqrt{\left(\frac{m\pi^2}{a}\right) + \left(\frac{n\pi^2}{b}\right)} \qquad (Hz) \tag{2-4}$$

$$\lambda_c = \frac{2}{\sqrt{\left(\frac{m\pi^2}{a}\right)+\left(\frac{n\pi^2}{b}\right)}} \qquad (m) \tag{2-5}$$

Where k_c is the cutoff wavenumber, m and n are the subscript of the particular TE or TM mode, a and b are the wide and narrow inner dimensions of the rectangular guide respectively.

Equation (2-4) depicts that the dimensions of a hollow metallic waveguide determine which wavelengths it can support, and in which mode. The larger the waveguide is, the lower the cutoff frequency for that waveguide is. Typically, for vast majority of applications, waveguides are designed for operation in its dominant mode,

which is the mode with the lowest cutoff frequency (f_c). For a rectangular waveguide with dimensions a>b, the lowest cutoff occurs for the TE_{10} (m=1, n=0) mode:

$$f_{c_{10}} = \frac{1}{2a\sqrt{\mu\epsilon}} \qquad (Hz) \tag{2-6}$$

Guide wavelength: The guide wavelength is defined as the distance between two equal phase planes along the waveguide i.e. the distance travelled by the wave in order to undergo a phase shift of 2 π. The guide waveguide is greater than the wavelength in free space ($\lambda_{freespace}$) and is expressed by :

$$\lambda_g = \frac{2\pi}{\beta} = \frac{2\pi}{k\sqrt{1-\frac{f_c^{\,2}}{f^2}}} = \frac{\lambda_{freespace}}{\sqrt{1-\left(\frac{\lambda_{freespace}}{\lambda_{cutoff}}\right)^2}} \qquad (m) \tag{2-7}$$

2.2.2 Waveguide losses

As electromagnetic waves propagate down a transmission line, it is continuously subjected to attenuation due to the lossy elements of the line, caused by conductor and dielectric losses. Attenuation is of practical importance in a lossy waveguide. The presence of these losses result in the propagation constant being complex in nature, which may be expressed as:

$$\gamma = \alpha + j\beta \tag{2-8}$$

Where α and β are the attenuation and phase constant respectively.

The attenuation is attributed to ohmic or conductor losses (skin effect) and dielectric losses, which are absorptive in nature and dissipate energy [37]. Hence, the total attenuation constant comprises of α_d which is the attenuation due to dielectric losses when the dielectric medium is lossy ($\sigma \neq \infty$) and α_c which is the attenuation due to conduction losses when the guide walls are not perfectly conducting ($\sigma_c \neq \infty$):

$$\alpha = \alpha_d + \alpha_c \quad (Np/m) \tag{2-9}$$

Attenuation due to conductor loss can be calculated using the perturbation method and depends on the field distribution in the guide.

Dielectric loss: Attenuation due to lossy dielectric applies to any waveguide propagating in TE or TM mode, with a homogeneous dielectric filling and is expressed by [33]

$$\alpha_d = \frac{k^2 \tan \delta}{2\beta} \ (Np/m) \tag{2-10}$$

Where,

$k = \omega\sqrt{\mu\epsilon}$ (real part of wavenumber without loss)

$\tan\delta = \frac{\epsilon''}{\epsilon'}$, also known as '*Loss tangent'* where ϵ' is the real part and ϵ'' is the imaginary part of the dielectric constant of the medium, respectively.

Conductor loss and skin depth:

At higher frequencies, resistive losses due to the conductive medium hold significant importance. Owing to skin effect, at high frequencies, the current tends to become distributed such that the current density is largest near the surface of the conductor. The skin depth is the thickness of the layer where the current density drops to 1/e the value on the surface. The penetration of the current flow i.e. the skin depth (δ), is formulated as:

$$\delta_s = \frac{1}{\sqrt{\pi f \mu_r \mu_o \sigma}} \quad (m) \tag{2-11}$$

Where, ρ is the resistivity (ohm meters),f is the frequency (Hz), μ_r and μ_o are the relative magnetic permeability of the conductor and permeability of free space ($4\pi \times 10^{-7}$ H/m) respectively. For microwave frequencies, skin depth tends to be a

small fraction of the conductor thickness. This being the region where current is concentrated and most of the resistive loss occurs, it is important that the conductivity of interior surface be kept high. Hence, waveguide interior surfaces are commonly plated with metals with high conductivity e.g. copper, silver, or gold.

The conductor loss is best treated using the perturbation method considering the power lost due to finitely conductive walls [33]. Thus, the attenuation due to conductor loss for the TE_{10} mode can be formulated as [33]:

$$\alpha_{c_{10}} = \frac{R_s}{a^3 b\beta\eta k}(2b\pi^2 + a^3k^2) \quad (Np/m) \tag{2-12}$$

Where R_s is the surface resistivity of the walls expressed as:

$$R_s = \sqrt{\frac{\omega\mu}{2\sigma}} \tag{2-13}$$

Where ω is the angular frequency, μ is the permeability of the dielectric and σ is the conductivity of the waveguide walls.

Other factors include non-absorptive losses such as mismatch losses which reflect energy, and losses due to radiation reflect which guide the energy away from the transmission line [37]. Mismatch losses take place as a result of discontinuity on a transmission line or difference in the termination impedance and transmission line impedance. Owing to load mismatches, no all the available from the generator is delivered to the load and is reflected. A measure of mismatch of such mismatch loss in dB is called *return loss (RL)* and is defined by

$$RL = -20log|\Gamma| \quad (dB) \tag{2-14}$$

The remaining power is transmitted along the waveguide, a measure of which is *insertion loss (IL)* which is expresses as

$$IL = -20log|1 + \Gamma| \quad (dB) \tag{2-15}$$

Additionally, radiation losses are caused by discontinuities or opening on the waveguide walls, resulting in the electromagnetic wave to radiate out of the line.

2.2.3 Effect of Conductor Roughness

Attenuation:

The surface roughness of a conductor affects the conductor loss with an increase in frequency, particularly at frequencies in multi-GHz range where signal skin depth becomes comparable to the scale of the conductor roughness [38]. The losses can be attributed to the fact that a small skin depth signal must travel along the surface of the rough conductor, effectively increasing the path length and conductor resistance. Hence the conductor exhibits even higher effective resistant than the predicted by the skin effect model, at high frequencies.

A numerical modeling of the effect of periodic square, rectangular and triangular grooves on conductor surface developed by S.P. Morgan based on power absorption analysis [39] has shown that as the skin depth of the signal approaches the height of the grooves, the conductor loss increase. The Hammerstad and Jensen Model based on Morgan's work incorporates the correction factor K_{SR} to the attenuation constant calculated for a smooth conductor [38]:

$$\alpha_{cond,rough} = \alpha_{cond,smooth} K_{SR} \tag{2-16}$$

$$K_{SR\_HJ} = 1 + \frac{2}{\pi} arctan\left(1.4\left[\frac{R_{RMS}}{\delta}\right]^2\right) \tag{2-17}$$

Where,

$\alpha_{cond,rough}$ = attenuation constant calculated for a smooth conductor in Np/meters

R_{RMS} = RMS tooth height in meters

δ = skin depth in meters

Since both $\alpha_{cond,rough}$ and K_{SR} are functions of frequency, the correction factor is small at either low frequencies, or when the ratio of R_{RMS}/δ is small (smooth conductor). The correction factor approaches 2 as its maximum, at high frequencies and rougher surfaces, and this predicts the 'saturation effect'. This model has proved

less accurate for frequencies above 5GHz for very rough copper [40]. This numerical model shows that the maximum effect that the conductor roughness has on the attenuation contact is double that for a smooth conductor, which however has been experimentally shown to be higher in [38].

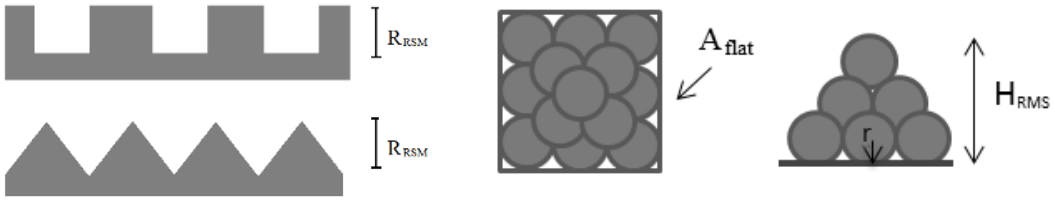

(a) (b)

Fig. 2-5 Conductor surface roughness based on (a) Morgan's Model (b) Huray's Cannonball Model

Morgan's model is the most popular model for surface roughness analysis, but it only takes into account periodic square, rectangular and triangular structures. While many other models have been proposed modelling the surface roughness[41]. Huray's Snowball Model is based on a non-uniform distribution of spherical shapes resembling "Snowballs" and stacked together forming a pyramidal geometry [42]. This model predicts that the correction factor, K_{SR} depends on the total area of snowballs stacked on unit area and not on the RMS height of roughness profile. However the snowball model relies on the use of many parameters to define the surface roughness profile, leading to the recent development of the Cannonball model [40]. The cannon ball model uses the concept of close-packing of equal spheres, and roughness correction factor is expressed as:

$$K_{SR} = 1 + 84\left(\frac{\left(\frac{(\pi r)^2}{A_{flat}}\right)}{\left(1 + \frac{\delta}{r} + \frac{\delta^2}{2r^2}\right)}\right) \qquad 2\text{-}18$$

Where,

δ= skin depth in meters
A_{flat} = area of square tile base surrounding 9 base spheres in sq. meter
R=radius of sphere in meters

In addition, the effect of random rough surface on the power absorption at microwave frequencies have been analyzed further using perturbation method and numerical method of moments method [43]. It is shown here that multiscale rough surface exhibit either no saturation, or occurring at much higher frequencies, and increase in conductor loss greater than a factor of two.

Phase constant:

The increasing in surface roughness also shown to have an effect on the phase constant, or effective dielectric constant. Rough surfaces exhibits more phase shift than a smooth surface corresponding to an increase in phase constant, or slowdown in phase velocity, as shown in [44], however the effect could not quantified. The increase in group delay due to surface roughness is suggested occur due to an increase in line inductance in [38]. However, roughness characterization by impedance computation done in [45] explains that the most probable cause for the substantial increase in dielectric constant is the capacitive effect of spikes on the surface of conductor.

2.2.4 Fabrication Challenges

Traditional rectangular waveguides are one of the main components used in military and satellite communication owing to the benefits of considerably reduced loss and leakage, high quality factor, and high power handling capacity at high frequencies. However, due to the inverse relationship of waveguide size and frequency, it becomes particularly difficult and costly to machine conventional waveguides of such small sizes with tight manufacturing tolerances [46]. Conventionally, geometrically complex, three-dimensional metal structures are manufactured with extensive micromachining that involves labour demanding metal-working processes, for instance, milling, drilling, lathing, shaping, brazing, Electron Discharge Machining (EDM), and other associated process demanding heavy

machinery and trained professionals. Using these conventional manufacturing techniques, the manufacturing volumes being low, and waveguide materials such as copper and silver are relatively expensive, overall manufacturing cost is expensive. Moreover, particularly at lower frequencies, the unwieldy size and mass of traditionally fabricated metallic waveguide pose as a disadvantage.

Owing to the ease of fabrication, 3D printing of waveguides has gained recent attention among researchers. Fused Deposition Modelling (FDM) and Stereolithographic 3D printing processes have been used to fabricate air-filled waveguides for millimeter-wave applications where the plastic/polymer printing is followed by commercial electroless plating and/or electroplating processes in [25], [26], [47]. However, the plating process involves the use of expensive, hazardous chemicals and requires other sets of equipment to be used, which defeats the purpose of rapid prototyping with ease. A binder jetting 3D printing technique has also been reported to fabricate a meshed metallic waveguide with metal powder [11]. [9] reports the use of Selective Laser Melting (SLM) technology to melt Cu-15Sn powder to build rectangular waveguides. These require expensive and specialized machines.

2.3 Waveguide Switching Mechanisms

The most commonly used commercially available waveguide switches incorporate rotor-based mechanical rotation [48][49] which despite low insertion loss, large OFF-state isolation and high power handling capabilities, are bulky expensive and relatively slow. RF MEMs waveguide switches [50]–[53] have been reported to provide miniaturization and high RF performance, but their packaging and long term reliability is yet to be investigated and remains a concern.

Fig. 2-6 Rotor-based Mechanical Waveguide switch [49].

Ferrite-loaded waveguide switches [54] offer the advantages of being smaller, lighter and faster, but are inferior in terms of performance. PIN diodes have also been incorporated for waveguide switching as reported in [55] but they present the need of fabrication complexity and device re-construction. Owing to the recent developments in microfluidic technologies and the popularity of using fluidic tuning in microfluidic devices, a water-based absorptive waveguide switch has been reported in [56]. However, absorptive switches in particular need to dissipate heat associated with the absorbed power.

2.4 Microfluidically Tunable Devices

2.4.1 Significance of Microfluidic-based tuning

The advent of microfluidics has led to the recent popularity of using microfluidic technology for reconfigurable RF components. Typically, RF component tunability is realized using either mechanical rotation, solid-state and varactor diodes or RF MEMs, as discussed in Chapter 2.3, which suffer from drawbacks of non-linearity, power losses, non-robustness, and fabrication complexity. The advancement in microfluidics has recently allowed researches to overcome these drawbacks and implement RF devices. By the advances in the

microfluidics field, fluidic control can be used to realize highly linear devices, and liquids being able to be circulated in channels, are capable of handling high-power RF inputs. Additionally, fluidic-based tuning eliminates possibility of surface damage [43], and can be employed in flexible, wearable devices [57], [58]. Moreover, liquid metal elements are capable of retaining their physical changes after removing the actuation force eliminating the need of continuous actuation. In addition, it offers ease of fabrication compared to other tuning mechanisms.

2.4.2 Review of Microfluidic Applications

At recent times, fluidic control for tuning microwave devices has attracted much attention owing to the advantages offered by fluidic control. The technology can be mainly divided into two categories owing the absorptive and reflective nature of the fluids in use [59]. Water based absorptive switches have been reported in [56], [59] , but they require careful design consideration to avoid mismatches, owing to the high dielectric constant of water. Dominantly, fluid based tunable devices substitute the essential metal elements, with a type of liquid metal to enable reconfigurability. Previously, Mercury, being the only naturally occurring metal that exists as a liquid at room temperature, was used as the tuning fluid [60], [61]. However, the high toxicity of mercury makes it unfavorable for the development of such devices. As a result, owing to their high conductivity, non-toxicity and liquid state at room temperature, commercially available liquid metal alloys such as Eutectic Gallium-Indium (EGaIn) and Galistan have attracted much attention for microfluidic-based configurability. While some examples of such work include the use of Galistan bridges to microfluidically reconfigurable antennas and filters [62]–[64], and microstrip patch antenna [65], tunable length monopole antenna [66] and SIWs [67][68] utilizing actuating EGaIn. The actuation mechanism for the liquid metal manipulation is either electrochemical or mechanical.

It should be also highlighted that, fluidic tuning, similar to that of latching switches, requires a one-time DC power consumption of less than 200 mW for

switching. This could reduce DC power consumption especially for the applications that the switch requires to stay in one state for a long time.

In this thesis, a 3D printed reflective waveguide switch is realized by fluidic tuning of liquid metal, to achieve reflective switching. The fundamental concept of reflective switches is to place liquid metallic posts in the critical path of RF signal and subsequently generate a short circuit. However, to our knowledge, their applications in waveguide structures have not been previously explored.

2.4.3 Challenges and limitations

Although microfluidic-based tuning of RF devices offers its advantages, it suffers from some challenges which need to be addressed. The first challenge is the choice of a suitable liquid metal considering its physical properties and RF performance. Following this is the challenge in handling and manipulation of the chosen liquid metal effectively.

Choice of liquid: Table 2-1 compares the physical properties of the available liquid metals with copper [58]. The naturally occurring liquid, Mercury, despite of having a low surface tension and low melting point is toxic and hazardous for health and environment. This led to the advent of low melting temperature alloys, particularly, gallium based alloys such as Galistan and Eutectic Gallium-Indium (EGaIn), which are non-toxic and have a much higher conductivity than Mercury.

Dealing with 'Skin' and residues: However, both EGaIn and Galistan suffer from its tendency to oxidize when in contact with oxygen, resulting in the formation of a thin oxide film ('skin') on the metal surface [69]. This surface oxide layer lowers the interfacial tension of the metal and causes unwanted adhesion, making it hard to handle. This tends to leave a skin residue when manipulating the liquid microfluidic channels, which adversely affect the RF performance of the device. In order to overcome this problem, a carrier liquid is required which would remove the skin layer and lubricate the manipulation of liquid metal through the microfluidic channels. The

RF properties, viscosity and toxicity of the carrier liquid play an important role, and have been studied [70][69]. A strong acid or base used as carrier liquid helps remove the oxide skin [71]; however the use of such harsh chemicals is undesirable for many practical implementations. A safer alternate option is naphthenic base oil, Hydrocal 2400 [65][69] and a low loss Teflon solution [72][73].

Table 2-1 Comparison of physical properties of Copper, Galistan, EGaIn and Mercury © 2015 IEEE [58].

	Copper	Galistan	EGaIn	Mercury
Melting Point (°C)	1085	-19	15.5	-38.8
Boiling point (°C)	2562	>1300	2000	357
Density (kg/m^3)	8960	6440	6280	1353
DC conductivity (S/m)	5.96×10^7	3.45×10^6	3.4×10^6	1.0×10^6
Viscosity (Pa.S)	-	2.4×10^{-3}	2.0×10^{-3}	1.5×10^{-3}
Surface Tension (N/m)	-	0.718	0.624	0.487

Injection and Manipulation: With the choice of liquid metal and carrier fluid made, the next step challenge is to effectively inject the liquid into channels. Prior to filling the channels, the liquid can be injected into a syringe by first withdrawing the carrier fluid into the syringe, followed by liquid metal, and ending with withdrawal of carrier fluid again to encapsulate the liquid metal [69].

The syringe is then attached to the microfluidic channel through fittings and pushed in and out of the channel. To achieve automated manipulation and positional control over the liquid metal in channels, the integration of micro-pumps [60] or electrochemical actuation [74] is vital.

3 3D printed waveguide

This chapter outlines the design and fabrication process of the waveguide using 3D printing fabrication technology. Following the waveguide fabrication rundown, the RF Characterization of the 3D printed waveguide is presented in this chapter. This work has been accepted for publication [75].

3.1 Design and Fabrication

Fig. 3-1 presents a block diagram outlining the core steps of the fabrication process. To begin the fabrication process, the primary step is modelling a waveguide, WR-42 (18 to 26.5 GHz), using ANSYS High Frequency Structure Simulation (HFSS) software [76]. The waveguide has a typical channel cross section of 10.668 mm x 4.318 mm with a 22.4 mm x 22.4 mm square flange. The waveguide is designed to have a plastic wall thickness of 1 mm. In order to print the waveguide channel and flange in a one-step printing process, support materials need to be added to any overhanging structure in the design, i.e. the flanges in this case. Hence, support structures are added to the design.

Next, the free-source software 'Slic3r'[77] is used to convert the CAD drawing of the waveguide structure into 'g-code', containing 2D sliced paths for the printer extruder to follow. Printing settings such as print center, scale, extruder and bed temperature, extruder, infill density and patterns, skirt and brim and layer heights need to be pre-loaded into Slic3r and necessary changes applied if needed before exporting the g-code.

The g-code is then sent to the 3D printer through the printer software 'Repetier-Host'[78] which commands the motors, relays and heaters to function accordingly. Following this, is the thermoplastic and ink printing processes, detailed in the successive sub-sections.

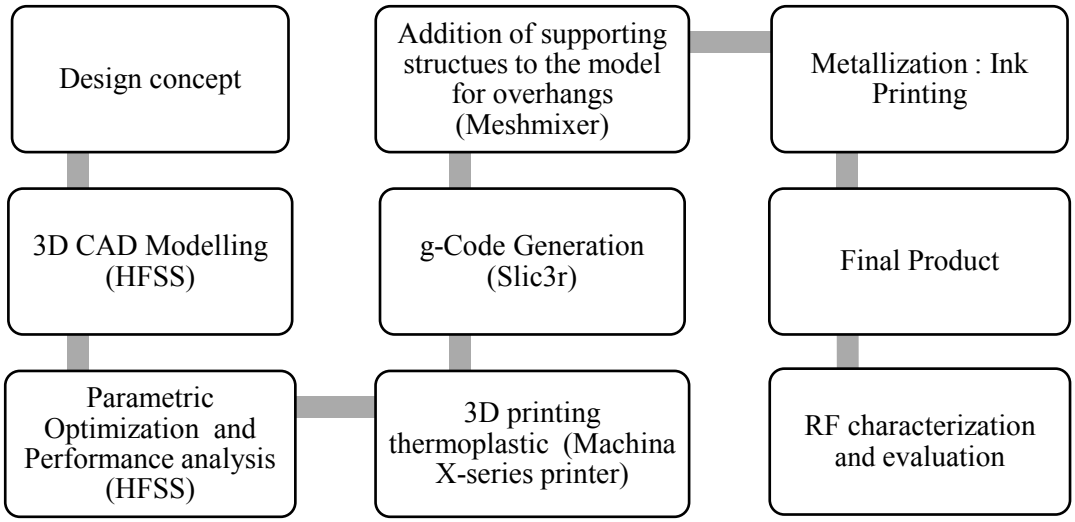

Fig. 3-1. Pictorial depiction of the device development process.

3.1.1 Thermoplastic Printing Process

A low-cost desktop 3D printer (X-series, Machina Corp [79]), retrofitted with a syringe and dispenser to add the capability of ink-printing [24] ,is used for the fabrication. The printer uses fused deposition modelling (FDM) technology to print thermoplastic ABS. Fused deposition modelling involves the extrusion of molten polymer filament, which is solidified and deposited on a heat bed. The filament is heated above its melting point, pushed down by rollers and material is extruded out of the nozzle, and the heated filament adheres to existing layers. The next slice of the part is deposited on top of the previous slice by the nozzle. In order to support overhanging parts, temporary support structures may need to be printed which can be broken off after build.

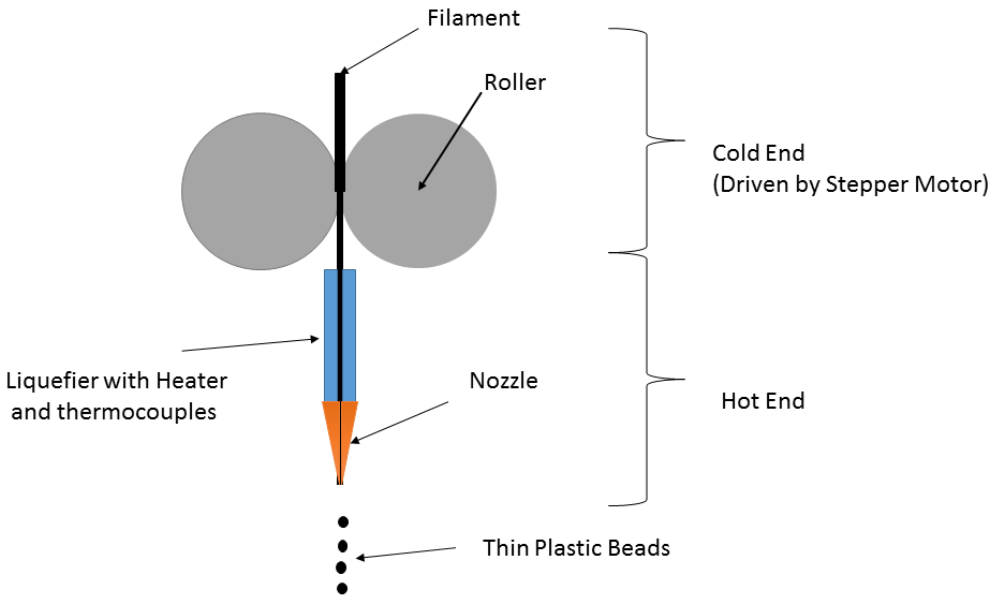

Fig. 3-2 Schematic of Fused Deposition Modelling Process [80].

Acrylonitrile butadiene styrene (ABS), which has a dielectric constant of 2.7 and loss tangent of 0.01, was used for the plastic waveguide body printing. The extruder, when heated to 220 °C, deposits ABS through 0.4 mm nozzle. In order to achieve one-step plastic printing, support materials are added to the CAD model using the software 'Meshmixer'[81] and printed simultaneously with the waveguide structure to generate a temporary platform supporting the overhanging top flange as shown in Fig. 3-3(a). The support materials are easily snipped off to obtain the final waveguide shape Fig. 3-3(b). The automatic support generation and part orientation is of importance because part orientation, and number and position of the supports will influence printing time and surface finish of critical areas [4].

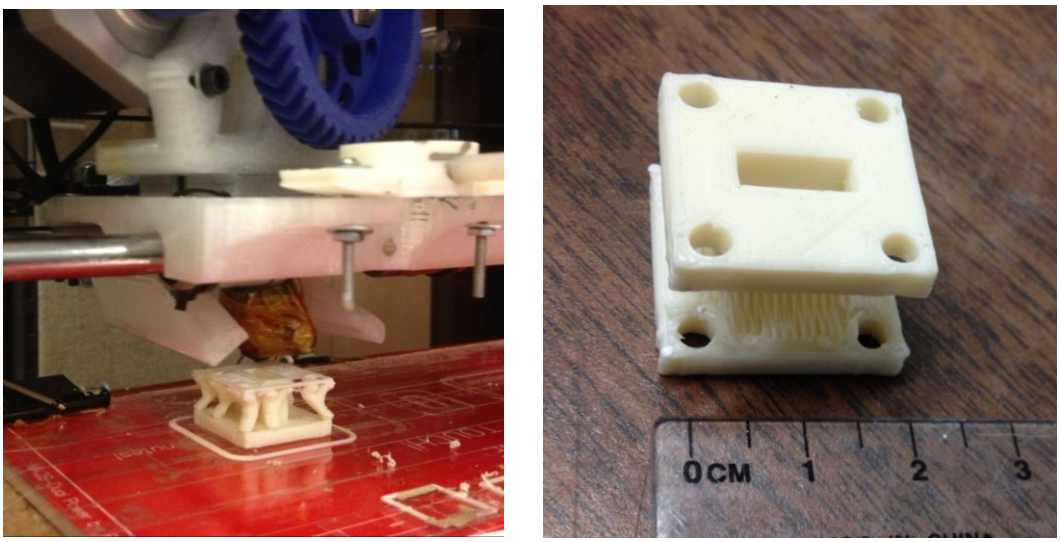

(a) (b)

Fig. 3-3 3D printed non-metallized waveguide body.

3.1.2 Ink Printing Process

The printed thermoplastic waveguide body only provides mechanical support for the device. Deposition of a conductive layer is necessary for RF functionality of the waveguide. As frequencies increase, conduction begins to move from an equal distribution through the conductor cross-section towards higher surface concentration, producing surface current, resulting in decreased skin depth (δ) as discussed in Section 2.2.2. Using equation (2-11), the skin depth is calculated to be 7.89 μm at 22 GHz. This highlights the fact that for a waveguide to operate at 22GHz, unlike conventional waveguides, the bulk of the conductive metal is not needed and a conductive film would be sufficient. This in return enables the use of the proposed 3D printing technique for developing waveguides and waveguide systems. Hence, following the plastic printing of the waveguide structure, in order to realize the conductive part of the waveguide, a low-cost silver conductive ink, AG-610 (Conductive Compounds) [82], was used to metalize the flanges and the interior walls of the waveguide that is responsible for transmission as shown in Fig. 3-4. The ink has a conductivity of around 2 x 10^5 S/m and takes 3 to 5 minutes at room temperature to dry or can be dried by forced air. The 3D printer had been customized

in the lab and equipped with a regulator, syringe and dispenser to also function as an ink printer for the metallization. Currently, some recently available commercial desktop 3D printers are equipped with plastic and ink printing capability for simultaneous printing [83]. Since the ink has the particle size of 18-20 microns, it is necessary to use a syringe with 10-20 times larger tip size for reliable and clog-free printing. Hence, a 510 μm syringe tip was used.

Fig. 3-5 illustrate the cross-sectional view and its corresponding top view schematic of the ink printing process. Following the plastic printing (Fig. 3-5(a)), ink is dispensed onto the flat flanges of the plastic waveguide, (Fig. 3-5(b)), using the dispenser and syringe. This is followed by printing ink around the perimeter of the inner channel until it overflows beyond the edges of the inner channel walls (Fig. 3-5(c)). Once the ink is dried completely, the waveguide is flipped vertically to print ink on the second flange (Fig. 3-5(d)), and left to dry, concluding the printing process. To achieve better conductivity, and ensure complete evaporation of the solvent in the ink, the printed bed is heated to 100 º C and inked waveguide is cured on it. Fig. 3-4(b) shows the final fabricated 3D printed plastic waveguides coated with silver ink. The over flowing technique used for printing/lining ink on inner surface of the waveguide, provides relatively smooth walls for smaller lengths of waveguides but, longer lengths, particularly longer than 1.5 cm long, tend to pose some challenges. One challenge with the overflow technique is ink sliding down the inner walls in tear-shaped blobs. Resultantly, a breach of uniformity of the surface coating is observed as shown in Fig. 3-6(a). This challenge requires to be further investigated for longer lengths and can be attributed to surface tension of different liquids. Cohesive forces between the molecules of the liquid ink pull the molecules closer together and tend to minimize the surface area [84]. On the contrary, adhesive forces between the ink and the ABS molecules allow the ink to stick and flow down the ABS walls. The tendency of the liquid to form droplets or spheres when flowing down the walls depends on the contact angle which is related to the relative strength of the cohesive and adhesive forces. Since the ink is observed to readily form spherical blobs when flowing down the walls, it can be concluded that the strength of the cohesive force relative the adhesive force is larger, leading to larger contact angle.

To overcome the challenge of non-uniform coating, the inner walls were overflown 2-3 times, ensuring maximum coverage of the walls with ink. Another challenge is the rounding of the corners and thickening of the edges of the inner walls as shown in Fig. 3-6(b), resulting in reduction of ink channel dimension. This was taken into account when printing the thermoplastic, by printing a larger channel than the actual, to compensate for the error.

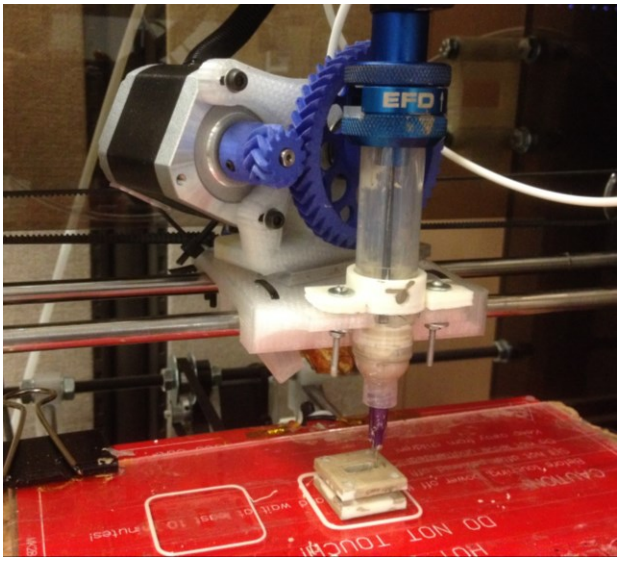

(a)

(b)

Fig. 3-4(a) Ink printing to achieve metallization on the 3D printed plastic waveguide (b) 3D printed and ink coated WR42 waveguide.

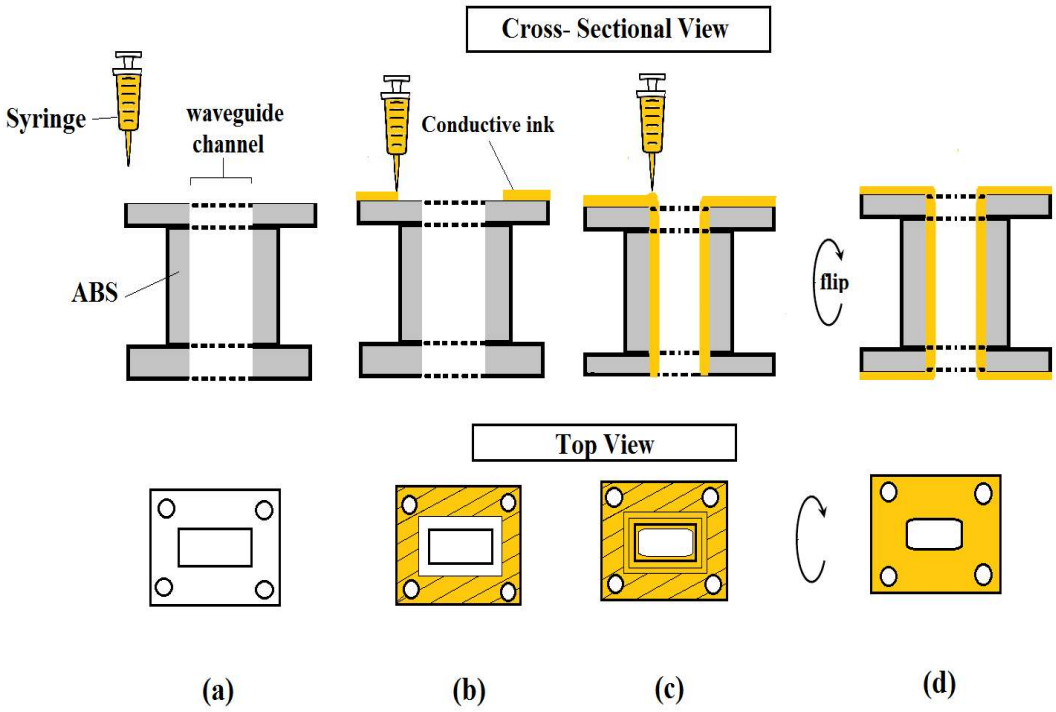

Fig. 3-5 Schematic outlining the ink printing process.

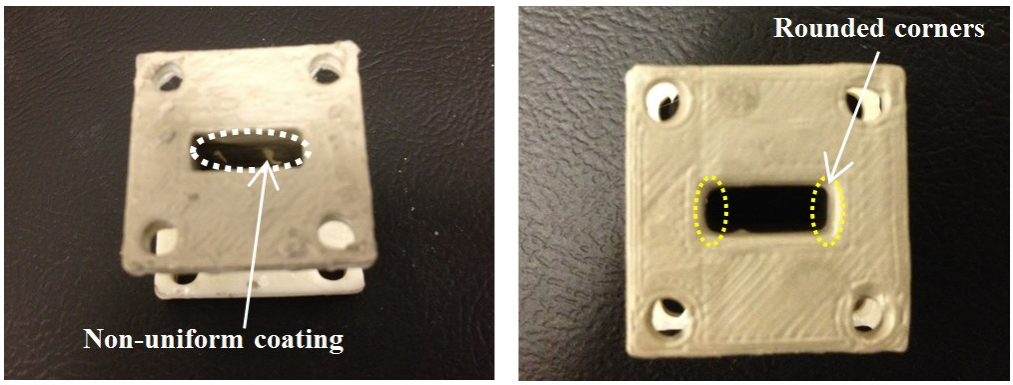

Fig. 3-6 Metal ink printing challenges in waveguides: (a) uneven coating of inner walls (b) rounded channel corners.

3.2 RF Characterization

3.2.1 Scattering Parameter Measurement

The Scattering parameters of the fabricated waveguide were measured using a PNA Agilent Network Analyzer, E8361C, after performing a two-port TRL calibration. The simulation and measured performance of a 1 cm long 3D printed, ink layered waveguide are presented over the entire K-band (18-26.5 GHz), in Fig. 5. The simulation takes into account conductivity of silver ink, and depicts an average insertion loss (S21) less than 0.08 dB and a return loss (S11) better than 77 dB, as shown in Fig. 3-7(a). The fabricated waveguide exhibits an insertion loss of better than 0.11 dB and an average return loss of better than 23 dB for the K-band in Fig. 3-7(b). The discrepancy between the measured and simulated results can be attributed to the surface roughness at the waveguide channel and flange contacts.

One should note that the surface roughness of the ink at the flanges can cause measurement challenges which are avoided here by filing the flange surface. Using a higher resolution 3D printer with a narrower nozzle for smoother printing of plastic walls would certainly reduce the existing surface roughness. It is also expected that the use of nanoparticle ink with a higher electrical conductivity improves the dissipative loss, and subsequently, the insertion loss.

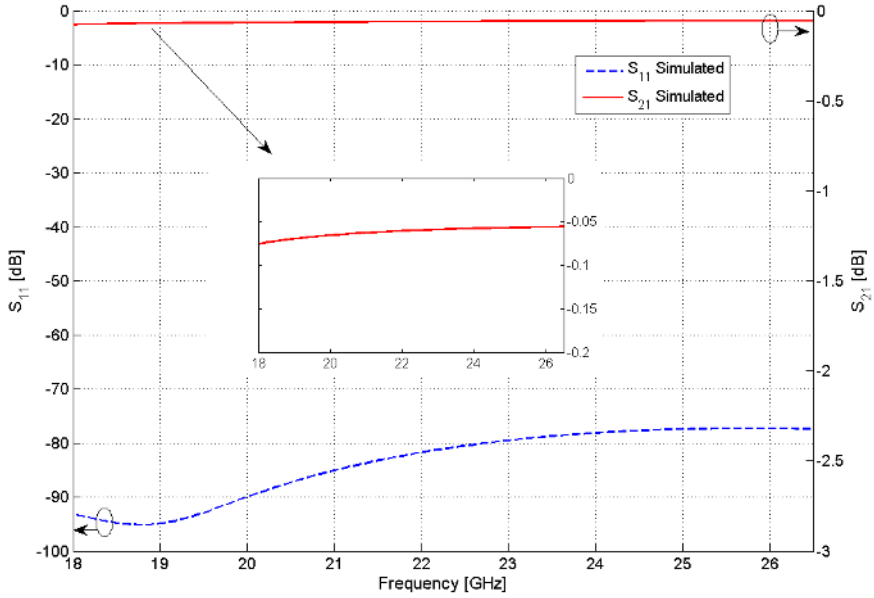

(a)

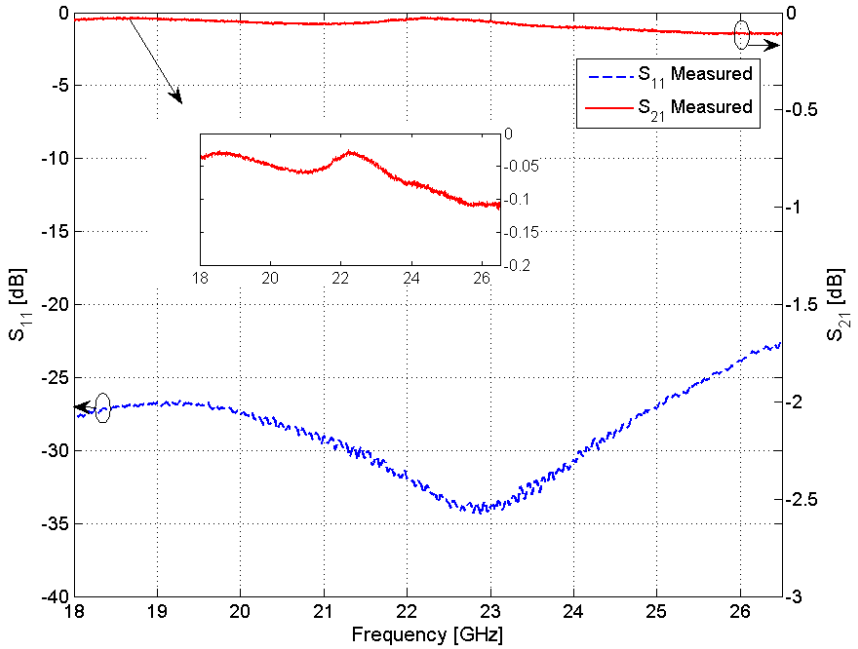

(b)

Fig. 3-7 Return loss and insertion loss of the 3D printed plastic waveguide coated with silver ink (a) Simulated and (b) Measured.

3.2.2 Loss Computation by multiline method

To characterize the performance of the 3D printed waveguide and determine its attenuation (α) and propagation constant (β), a multiline method [85], [86] is performed, as detailed in Appendix B. To conduct this method, two lengths of line, 1cm and 2cm were measured and a MATLAB code is used to extract these parameters from the measured S-parameter. Fig. 3-8 present the attenuation and phase constants of the ink waveguide extracted from the simulated and measured S-parameters of two lengths of waveguide. The attenuation constant, computed from measured data, shows slight variation from simulated data, showing an average attenuation of 0.27 dB/cm. The attenuation loss is composed of dielectric and metallic loss. Since this is an air-filled waveguide, it can be assumed that the main contribution to attenuation loss is due to the metallization of the waveguide. The measured phase constant is found to be closely comparable to that computed from simulated data.

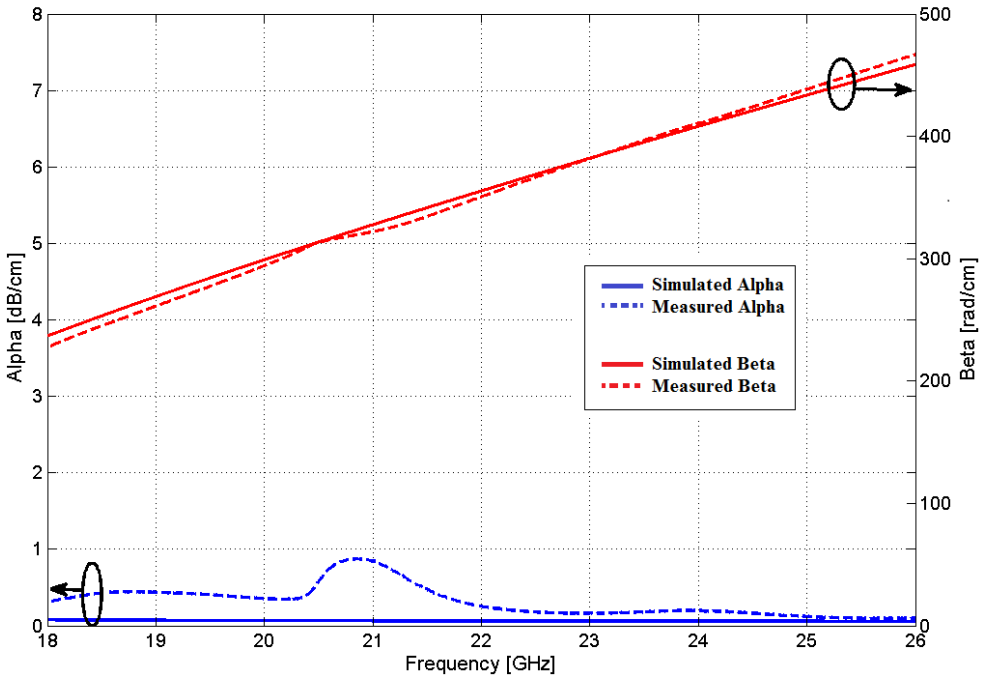

Fig. 3-8 Attenuation constant (α) and phase constant (β) calculated from two lengths of waveguide line using simulated and measured S-Parameters.

3.3 Summary

A fully 3D printed plastic and metal-ink rectangular waveguide (WR42) is presented in this chapter. A detailed process flow for the thermoplastic printing and ink printing dispensing process is outlined here. The measured total insertion loss of the 3D printed waveguide is in good match with the simulations showing better than 0.11 dB/cm for the entire K-band and an average return loss better than 25 dB for the entire K-band. The 3D printed waveguide is characterized and its attenuation and propagation constants are computed for the K-Band using a multi-line technique. The discrepancy between the measured and simulated results can be attributed to the surface roughness of the printed plastic parts, flange contacts and ink conductivity.

4 Microfluidically Controlled 3D printed Waveguide Switch

The objective of this thesis is to exhibit the potential of 3D printing technology to manufacture functional RF devices. In this section we further utilize such 3D printed waveguides to develop waveguide switches integrated with microfluidically controlled conductive metal. In this chapter, the switch concept will be developed, applied and incorporated into the 3D printed waveguide presented in Chapter 3.

4.1 Design analysis

The elemental concept of the microfluidically controlled reflective switch is to attain a short circuit by placing liquid metallic posts in the critical path of the incident RF signal. Having the liquid metal microfluidically propelling in and out of the waveguide cross-section, thus blocking and allowing wave propagation, creates the switch OFF and ON State respectively. In a practical scenario, this can be achieved by moving plugs of liquid metal, contained in tubes, in and out of the waveguide, using pumps.

For the liquid metal, the switch design utilizes EGaIn, an eutectic metal alloy made by mixing 75% Gallium and 25% Indium, with a resultant conductivity of 3.4 x 10^6 S/m [71] and a melting point of ~15.5 °C. EGaIn has an inert tendency to react with air and form a surface oxide layer, which could lower the interfacial tension of the metal and cause unwanted adhesion to the walls of the tube. PTFE tubes, having a dielectric constant ($\boldsymbol{\varepsilon_r}$) = 2.1 and, loss tangent ($\tan\delta$) =0.0015 [87], are chosen in this work as they offer low insertion loss, in addition to having low coefficient of friction & hydrophobicity. To prevent further stiction, the tubes were initially filled with carrier liquid, Hydrocal 2400 oil [69] , having the dielectric constant of 2.31, and the loss tangent of 0.05. The oil acts as a slip layer, preventing the contact of the metal to the tubes and air. Furthermore, the oil layer also encloses EGaIn in the tube

and its high viscosity (442.44 cSt at 40°C) aids the manipulation of the EGaIn plug using pumps.

A model of the switch was designed in HFSS and a parametric study was performed by simulating different configuration of tube sizes and the number of tubes, in order to achieve a realizable configuration providing optimal performance both in the ON State and OFF State . The electric field analysis for TE_{10} mode of the designed rectangular waveguide from Section II revealed that the fields are concentrated at the center of the channel, as shown in Fig. 4-1. Hence, by theory, insertion of centered, metallic cylindrical posts, parallel to the dominant –mode electric field, as illustrated in Fig. 4-2, would cause maximum hindrance to the input wave. Principally, the switch design can be represented into its equivalent circuit model as shown in Fig. 4-3. The PTFE tube wall separates the liquid metal from being in direct contact with the waveguide's top and bottom walls creating gap capacitances C_{g1} and C_{g2}. The liquid metal post, on the other hand, introduces an inductance of L_m. It is expected that the highest isolation is achieved at the frequency band where the overall circuit is resonating.

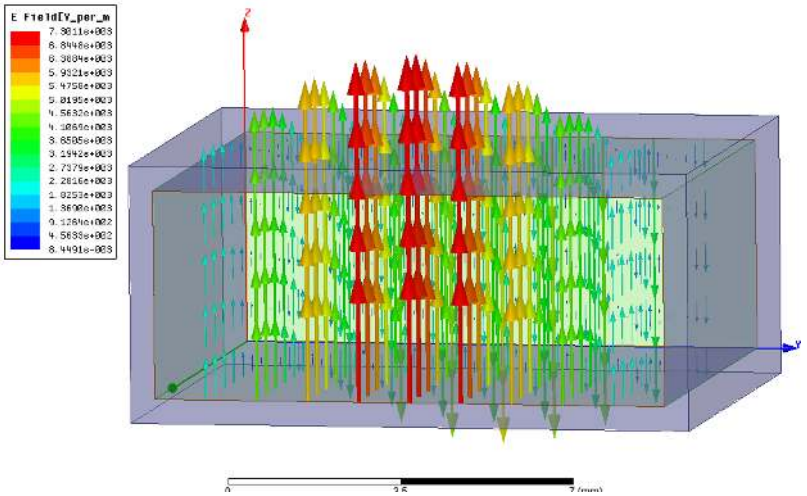

Fig. 4-1 Simulated plot of Electric field inside an empty hollow waveguide

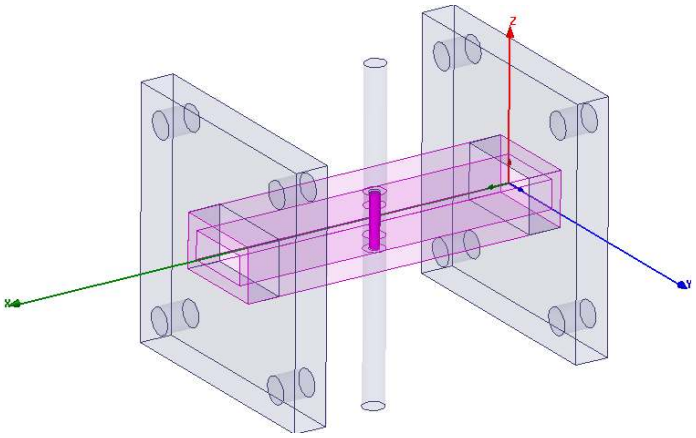

Fig. 4-2 Design schematic of waveguide with one tube penetrating through the center of broad wall.

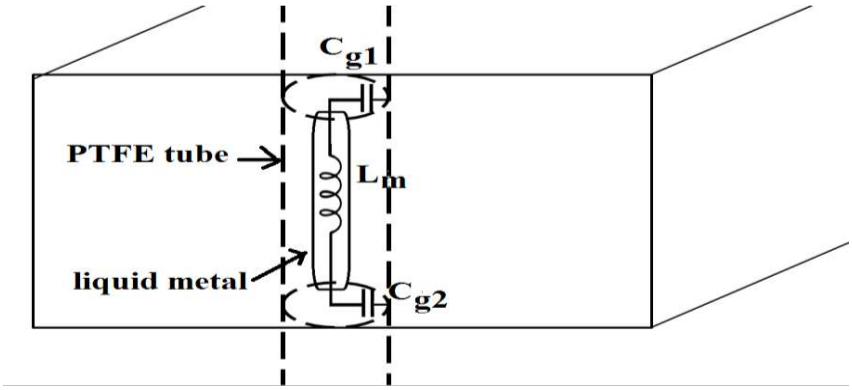

Fig. 4-3 Equivalent L-C circuit representing the waveguide switch.

4.2 Parametric study

In order to study the factors affecting the performance of the switch, HFSS simulations were performed for two main parameters. The first parametric analysis was carried out with just one tube placed at the center of the waveguide channel, as shown in Fig. 4-2 and the insertion and isolation are compared for three different tube sizes. Table 4-1 lists the inner and outer diameter of the three tube sizes and other parameters considered for simulation. The inner diameter of the tube is indeed the diameter of metal post in OFF State and oil in the ON State .

Table 4-1 : TUBE PARAMETERS

Tube	Inner diameter (mm)	Outer diameter (mm)	Dielectric constant (ε_r)	Loss tangent (tan δ)
Tube A	0.25	1.59		
Tube B	0.5	1.59	2.1	0.0015
Tube C	1.55	3.175		
Oil	-	-	2.31	0.05

Fig. 4-4(a) compares the simulated scattering parameters for the three oil-filled tube size in the ON State. Comparing insertion loss tube C with a comparatively larger inner and outer diameter exhibits higher insertion loss, owing to thicker walls and higher oil content in comparison to tube A and B. Fig. 4-4(b) illustrates the simulated OFF State isolation for the three tubes. For all the of the a wide band isolation is achievable and it is observed to be better at different specific frequencies for each tubes B and C, where S21 appears to be resonating.

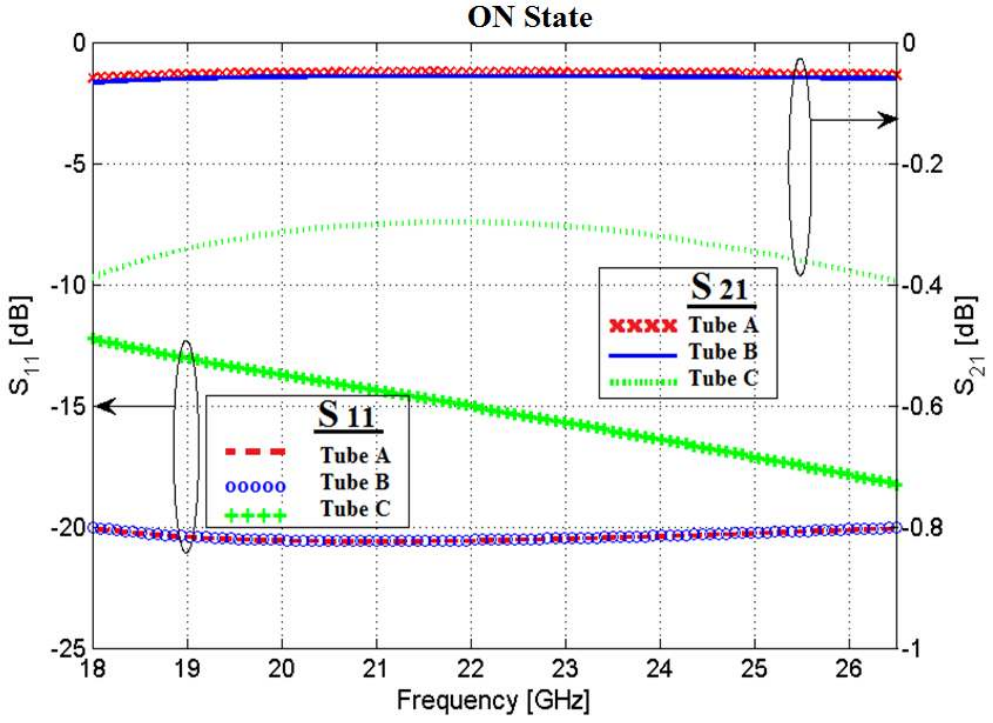

(a)

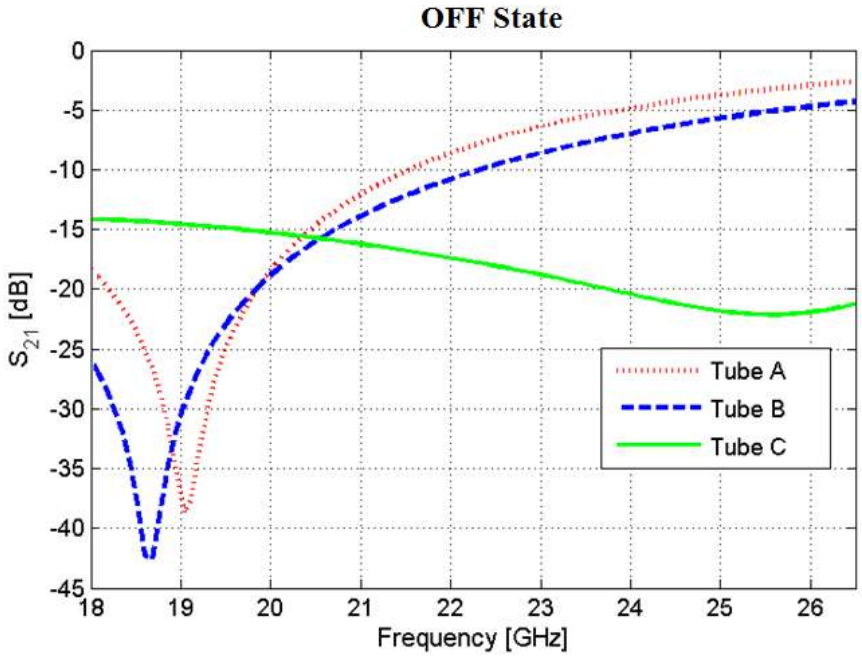

(b)

Fig. 4-4 Effect of tube size on the (a) ON State S-Parameter and (b) OFF State isolation.

Further simulation was performed to observe the effect of increasing the number of tubes (Tube size B) with liquid metal as shown in Fig. 4-5. The results plotted in Fig. 4-6(a) depicts that increasing the number of tubes increases the insertion loss (S21), although not considerable. However, for the OFF State , increasing the number of tubes does not necessarily increase isolation, but causes the overall circuit resonance to shift. Hence, to achieve high isolation at a desired frequency band, the location of the resonance should be optimized. Fig. 4-7 demonstrates the plotted electric field inside the waveguide, with and without the liquid metal plug, i.e. the OFF and ON States, respectively. As conceptualized, the plots reveal that the electric fields propagate freely when the tubes are filled with oil only in the ON State (a), while they are hindered by the presence of liquid metal generating OFF State (b).

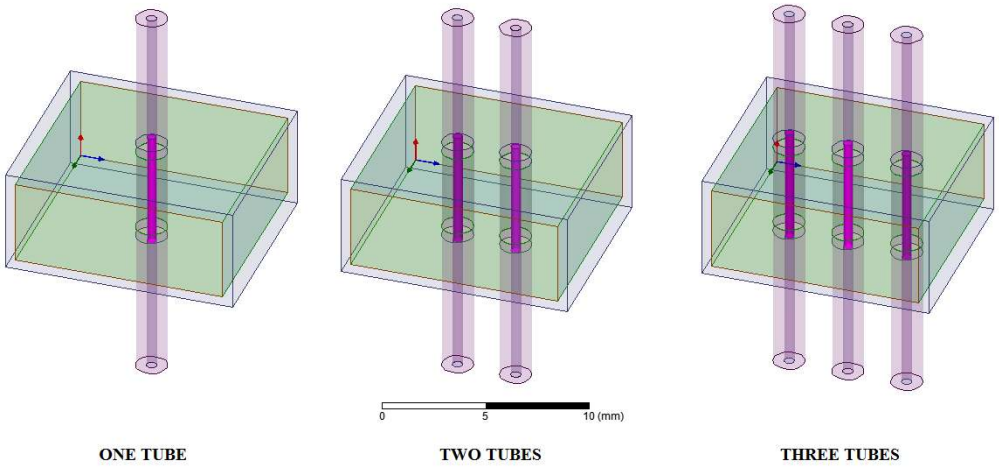

Fig. 4-5 Simulated Configurations of the switch with different number of tubes (Tubr B).

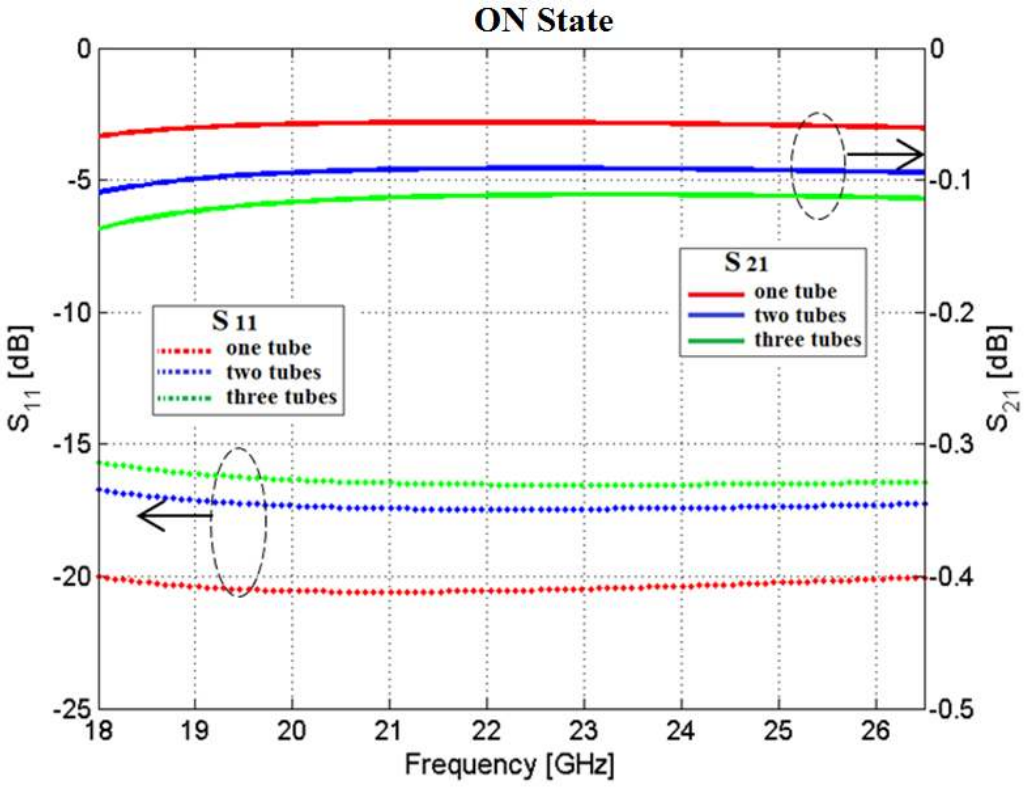

(a)

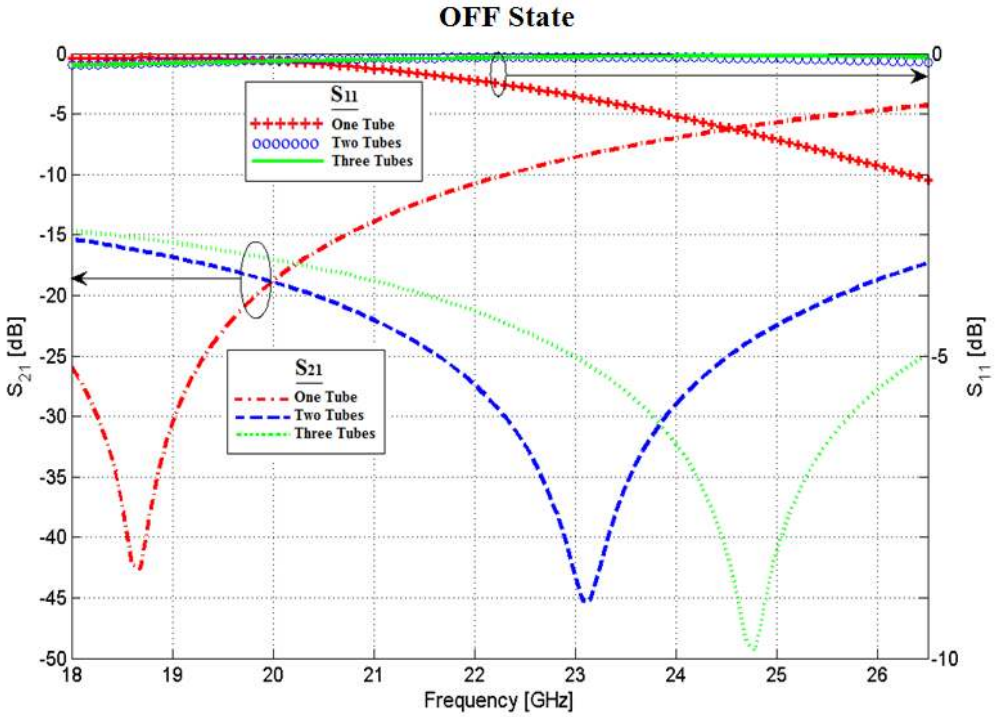

(b)

Fig. 4-6 Effect of number of tubes on the S-Parameters of the switch in the (a) ON State and (b) OFF State

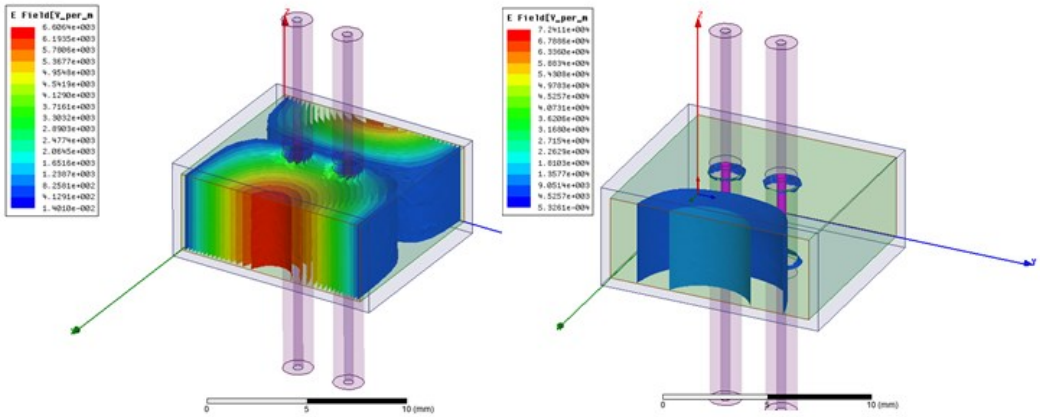

(a) (b)

Fig. 4-7 Electric field inside the channel of the switch in the (a) ON State and (b) OFF State at 18GHz.

4.3 Switch Assembly

Inspecting the simulated design parametric study, application of two tubes provides optimum isolation achieved for the frequency band of interest. Therefore, considering two tubes incorporated in a 1cm waveguide was chosen for the final switch assembly. The switch, as designed in Fig. 4-8(a) was incorporated by drilling two holes on the broad wall of the 3D printed waveguide, positioned at the center, and separated by 1.3 mm. Two PTFE tubes, each having an inner-diameter of 500 µm, were inserted through the holes as shown in Fig. 4-8(b). Hydrocal 2400 oil was first injected into the tube using a syringe, followed by liquid EGaIn, and then oil again to encapsulate the liquid metal plug.

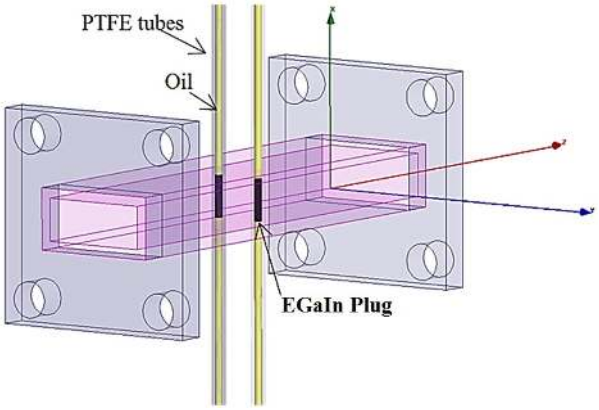

(a)

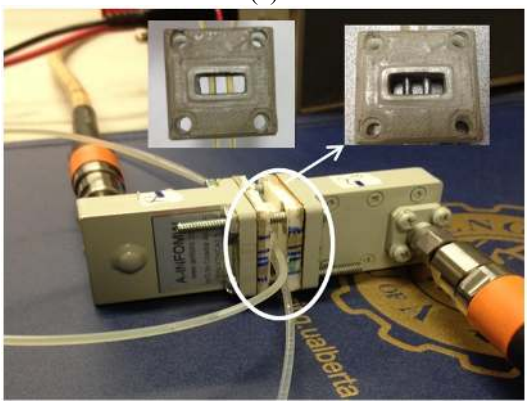

(b)

Fig. 4-8 3D printed microfluidically controlled reflective waveguide switch (a) CAD model (b) Practical implementation of the switch connected between waveguide to coax adaptor test heads.

For testing purposes, the microfluidic pumping action was initially performed using syringe pumps in an open loop system. However, due to the bulkiness of the syringe pumps, Bartel's piezoelectric Diaphragm micropump (mp6) [88] was used for a more compact setup as shown in Fig. 4-9. The piezoelectric diaphragm pump functions by deforming a brass membrane up and down using a piezo ceramic mount, by voltage application. With every stroke, the liquid is sucked into the pump chamber, filled again, and pushed out. This allows an integrated size and closed loop connection, unlike syringe pumps that require an open loop pumping mechanism. The pump is connected to a control unit, mp6-OEM, which generates up to 235 V peak to peak voltages from a 3-5 V supply. The controller drives the mp6 at adjustable performance in a package similar to an integrated circuit. The power consumption is less than 200 mW. Inherently, the pump has a maximum flow rate of 7ml/min for water. However, as Poiseuille's Law states, flow rate being inversely proportional to viscosity, the pumping rate is significantly reduced due to the high viscosity of the oil and liquid.

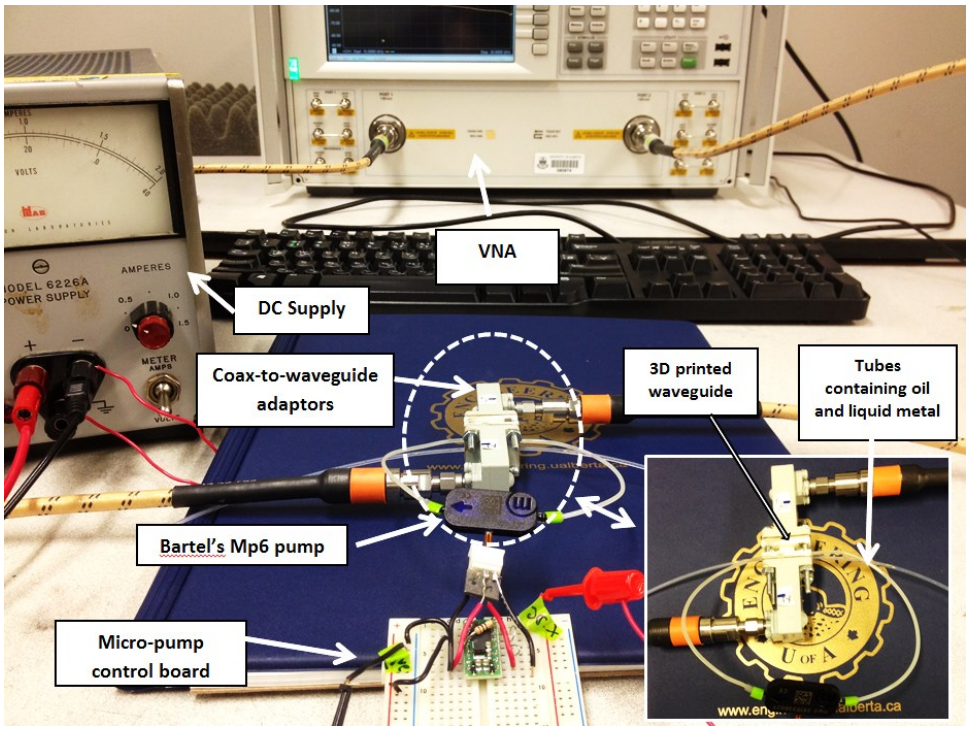

Fig. 4-9 Measurement setup for the 3D printed microfluidically controlled waveguide switch.

To achieve bi-directional pumping for the to and from actuation of the liquid metal through the tube, the setup could be modified to constitute a combination of two pumps in parallel paths, so that there is one pump for each direction, as shown in Fig. 4-10. Two active 2/2 way valves would enable direction selection. This structure allows pushing the liquid metal in and out.

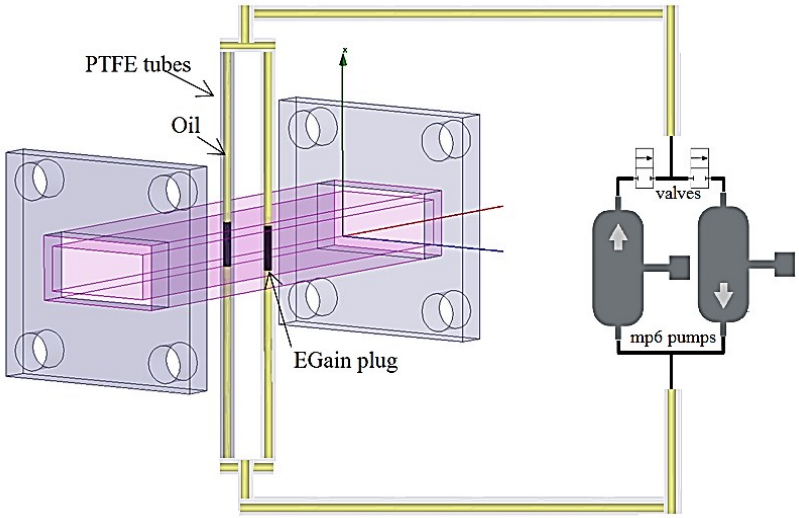

Fig. 4-10 The proposed waveguide switch set-up for bidirectional pumping of liquid metal.

4.4 Measurement and Results

4.4.1 RF Performance Analysis

The measured ON State performance of the switch is shown in Fig. 4-11(a) presents an insertion loss of 0.51 dB for the entire band, which is slightly higher than the simulated loss. To understand the source of the added loss, the effect of the drilled holes (no tube), empty tubes, and oil-filled tubes are separately demonstrated. It is expected that by replacing the tube with one with thinner walls, and made out of material with lower loss tangent, better ON State performance can be obtained. The

insertion loss could further be reduced by replacing the oil (ε_r = 2.31, tan δ =0.05) with a Teflon solution (ε_r = 1.89, tan δ =0.00025). The ON State return loss of the switch is better than 13 dB for the entire band. As it is shown in the figure, the insertion of the tubes also impacts the matching which can be potentially improved by changing the type of the tubes. Fig. 4-11(b) shows the OFF State performance of the switch, exhibiting an isolation of better than 15 dB for the entire band, and better than 20 dB in the band 21-25.4 GHz. The simulation and measured results agree well and illustrate high potential of using 3D printed waveguides integrated with liquid metal for waveguide switch prototyping.

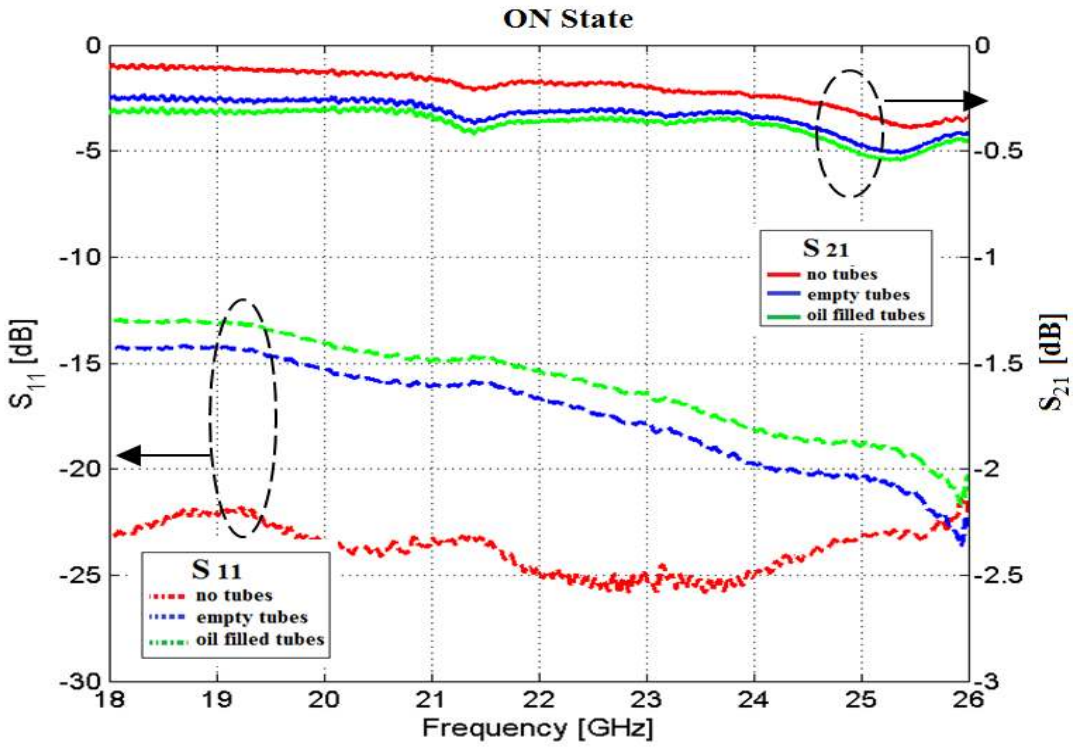

(a)

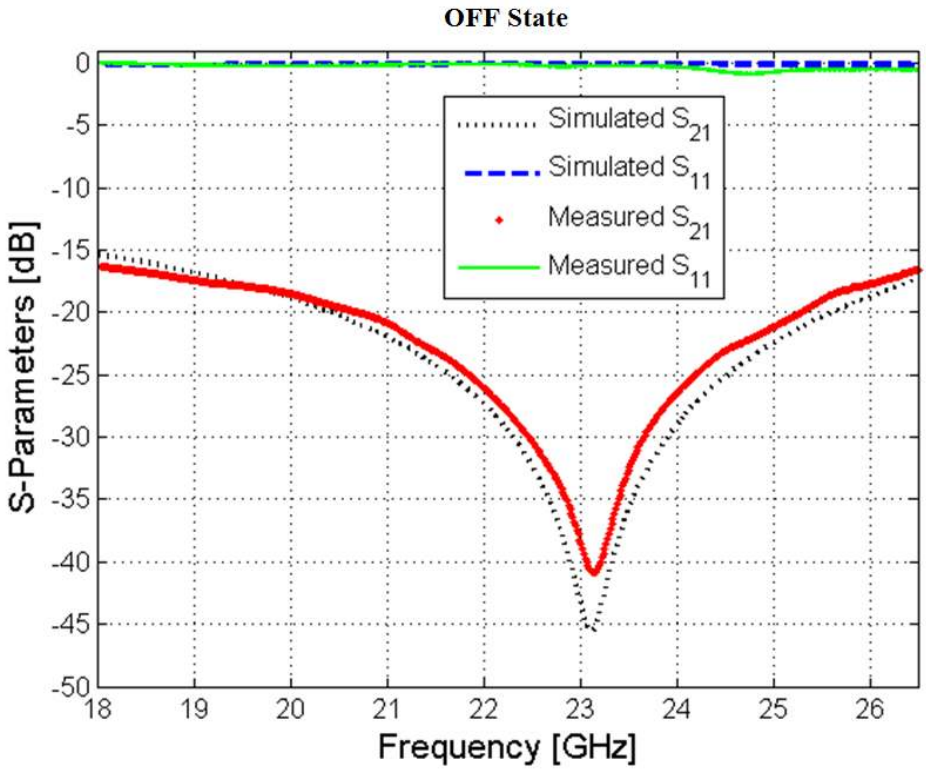

(b)

Fig. 4-11 Measured S-parameters of the microfluidically controlled waveguide switch exhibiting (a) ON State performance of the switch with no tubes, empty PTFE tubes, and oil-filled tubes (b) OFF State performance with liquid metal pumping.

4.4.2 Temperature Stability

To achieve better understanding of the proposed structure operation in real world application, we have looked into the effect of temperature variation on the switch operation. We consider two cases of ON and OFF States.

Switch at ON State: Primarily, measurements were performed to study the effect on the performance of the switch at ambient temperatures higher than room temperature. ABS has a glass transition temperature of approximately 105 °C, and does not begin to soften below that point. Hence, the waveguide structure holds its shape and form till 105 °C. The setup for the measurement is shown in Fig. 4-12, where the waveguide switch is placed on a hot plate that is heated gradually, while the S-Parameters of the device are measured using a VNA.

An infra-red (IR) thermometer [89] is used to measure the surface temperature of the hot plate, adaptors and the thermoplastic plastic waveguide, simultaneously. It is observed that the outside surface temperature of the 3D printed thermoplastic waveguide is generally 12-20°C lower than the center of the hot plate, owing to the inherent insulating properties of thermoplastic, ABS. The heated hot plate acts as the ambient, which conducts heat from the hot-plate to the adaptors and eventually to the thermoplastic waveguide. Fig. 4-13 shows the performance of the switch in the ON State plotted against the temperature of the plastic waveguide's outer surface and the coax-to-waveguide adapter surface, ranging from room temperature to 67.6 °C and 81.0 °C respectively. The result exhibits inconsequential variation in insertion loss with increasing temperature.

Switch at OFF State: The liquid metal, EGaIn, used for switching, has a melting point of ~15.5 °C; hence, it retains its liquid form at temperatures above 15.5°C. Hydrocal 2400 Oil, however, is reported to have a viscosity of 442.44 cst at 40 °C which reduces to 22.75 cst at 100 °C. Hence as the temperature increases, the oil becomes less viscous. Hence, in an open loop pumping system, the switch is prone to noticeable variation in its OFF State performance as shown in Fig. 4-14(a). This is improved with the use of a closed loop pump set up. Fig. 4-14 (b) shows the OFF State performance with varying temperature, when the fluidic tubes are connected to the pump in a closed loop. Although, slight variation is still noticed as the temperature rises, the difference is quite insignificant.

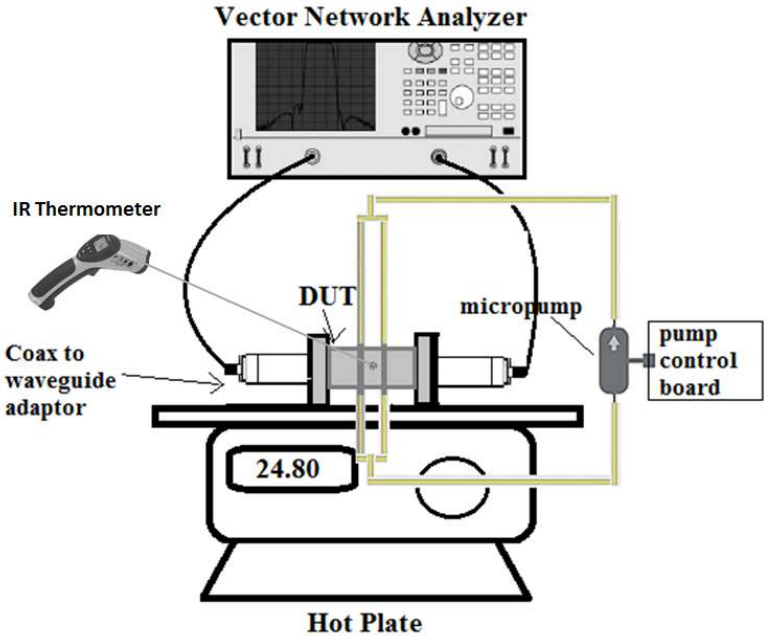

Fig. 4-12 Measurement setup to study the effect of Temperature on the 3D printed microfluidically controlled waveguide switch.

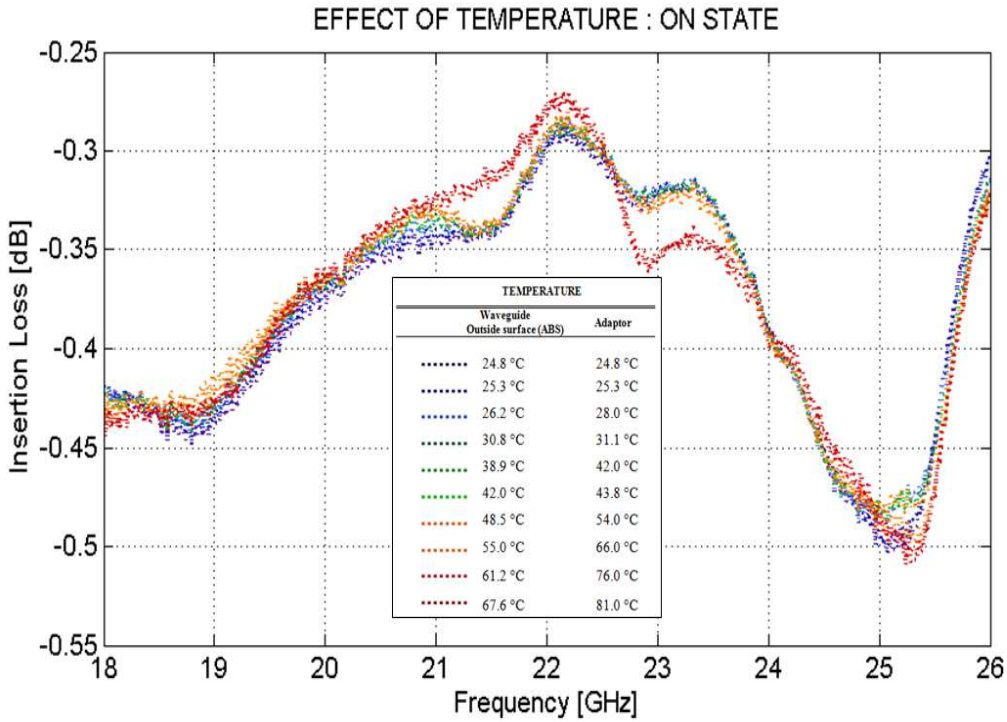

Fig. 4-13 Measured effect of temperature on the ON State insertion loss.

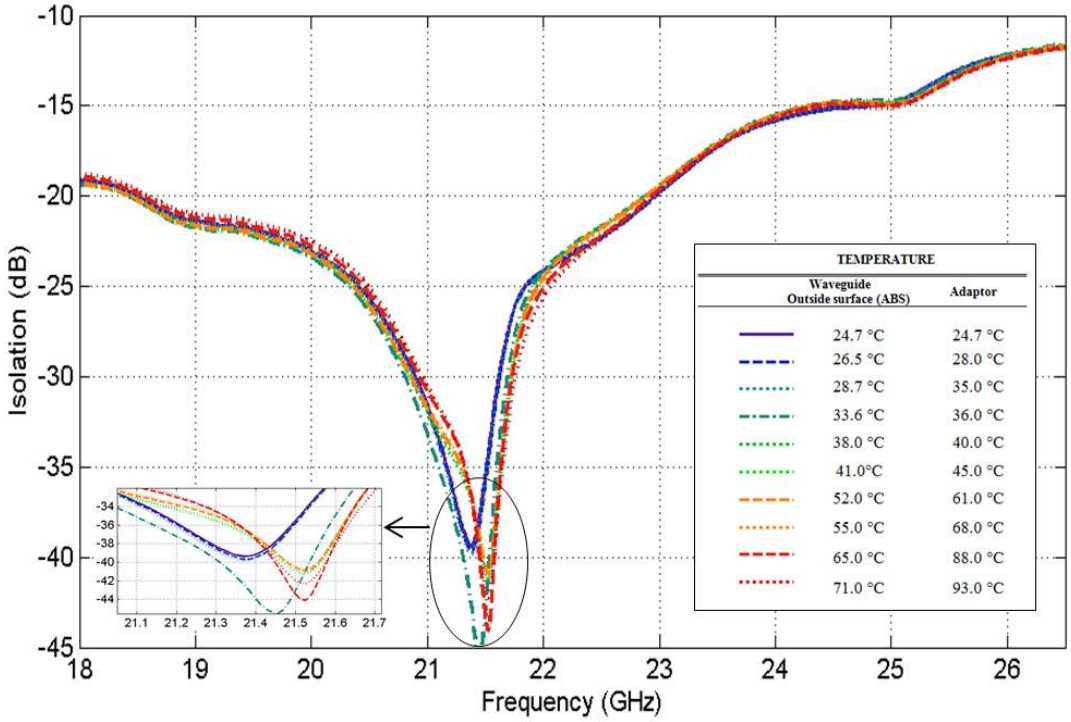

(a)

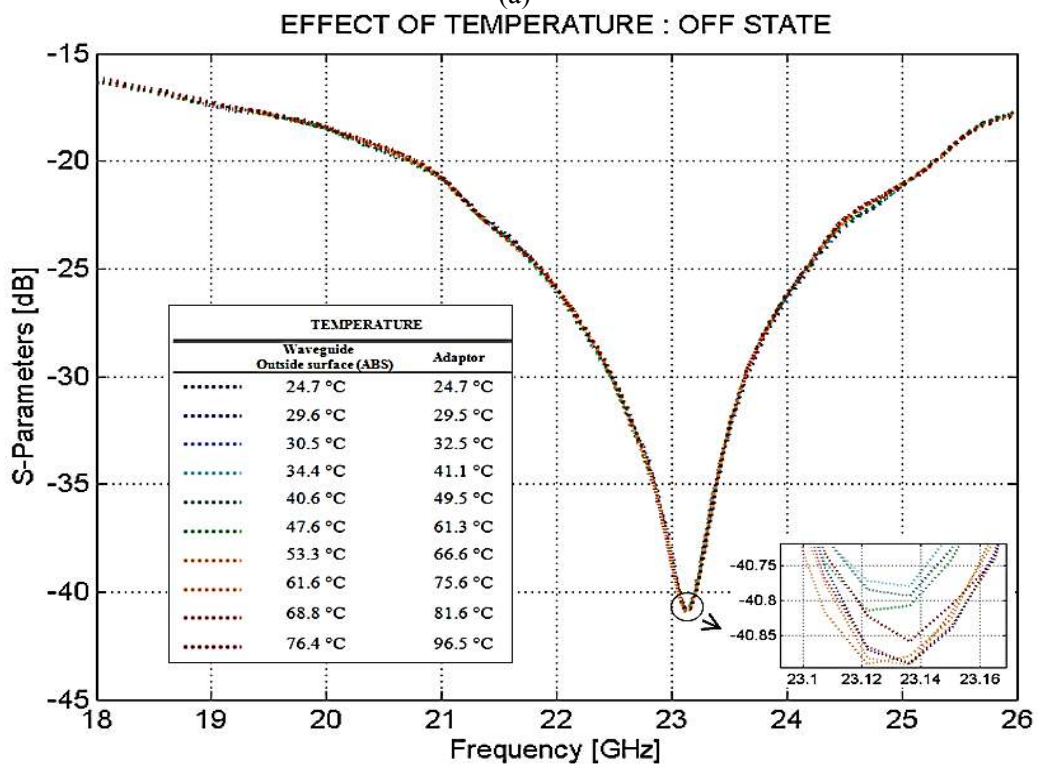

(b)

Fig. 4-14 Measured effect of temperature on the OFF State isolation with (a) Open-Loop and (b) Closed-loop fluidic switching.

Discussion on operating temperature span: The liquid metal has a melting point of 15.5 °C, while the Hydrocal oil has a pour point of 0 °C. At low temperatures, the metal and the oil would begin to solidify, affecting the ability to switch between ON and OFF States. For operation at lower temperatures, an alternative to EGaIn is to use the metal alloy Galistan, which melts at -19 °C, and has a conductivity of 3.46 x 10^6 S/m [58].

Fig. 4-15 shows the measured performance of the waveguide microfluidic switch incorporating both EGaIn and Galistan. Both metals exhibit an isolation of more than 15 dB for the entire band. The deviation of the results for EGaIn and Galistan around 23 GHz can be attributed to the height of liquid metal in the tubes. Lengths of the EGaIn plugs used for the switch are approximately 5.2 mm each while those of Galistan are ~ 8 mm leading to different resonating frequencies. Additionally, Hydrocal 2400 can be replaced with other Hydrocal Grades with pour points that can go to as low as -80°C [90], for the switch operation at temperatures much below room temperature. Alternatively, Teflon solution (Teflon AF 400S2-100-1, 1% Teflon powdered resin dissolved in 3M FC-40 from DuPont) [91] can also be used.

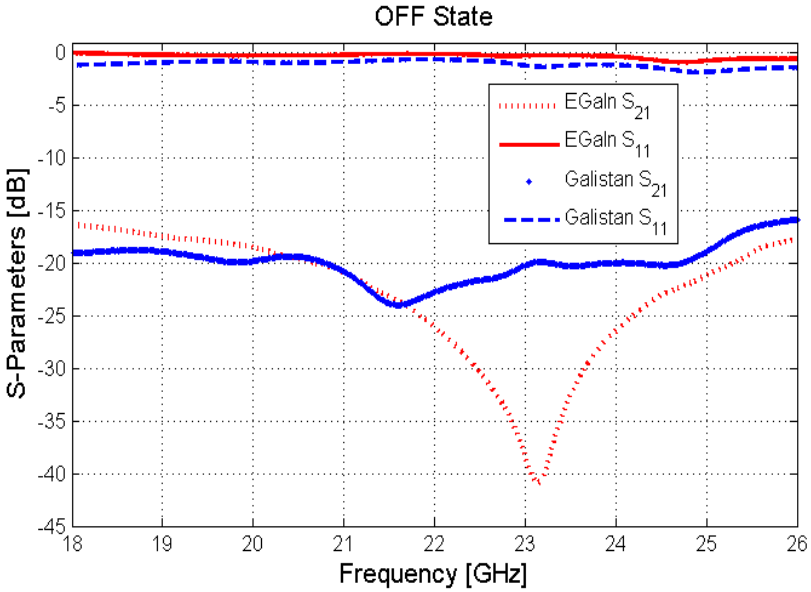

Fig. 4-15 OFF State switch performance with EGaIn and Galistan.

4.4.3 Studies on Switching Speed

One of the major concerns with microfluidically controlled devices is the tuning speed, which mainly depends on the volumetric flow rate of the fluid. For the setup presented in this work, the speed was measured to be 0.73 mm/sec, with our choice of tube and oil carrier. To measure the speed, the movement of a 4-mm long metal plug in a marked Teflon tube is video recorded and the time stamps on the video for when one end of the liquid metal crosses the markings are used to measure the velocity. This test was repeated with varying distances between the 'start' and 'stop' marks and the average speed is reported.

Due to the liquid viscosity responsible for the friction between the tube and the liquid, the velocity profile of laminar flow in a pipe is parabolic with a maximum at the centerline and minimum at the pipe wall [92]. Applying these boundary conditions, for laminar flow, the volume flow rate (Q_{vol}) of an incompressible fluid with viscosity η through a horizontal pipe of length L can be determined using Poiseuille's law.

$$Q_{vol} = \frac{\pi(P_1 - P_2) \times {R_i}^4}{128\eta \times L} \tag{4-1}$$

Where R_i is the tube's inner diameter, $(P_1 - P_2)$ is the pressure difference across the pipe length, and η is the viscosity of the liquid. Consequently, the average velocity of the liquid (v) can be calculated using (4-2).

$$v = \frac{Q_{vol}}{Area} = \frac{(P_1 - P_2) \times {R_i}^2}{8\eta \times L} \tag{4-2}$$

As shown by equation (4-2), the velocity is directly proportional to the pressure difference and the square of the inner diameter of the tube (${R_i}^2$) while inversely proportional to the fluid viscosity and the length of the tube (L). Based on (4-2), using lower viscosity carrier fluid such as Teflon solution is expected to

dramatically improve the speed compared to our setup presented here. It should be noted that the pressure drop is dictated by the pump's power rating [92]. Hence the pump choice also becomes highly critical.

4.5 Summary

In this chapter, a microfluidically controlled waveguide switch, using liquid metal, was proposed, implemented and measured, as an application of the 3D printed waveguide depicted in Chapter 3. The propose concept of realizing a reflective microfluidic switch using liquid metal alloys is detailed is detailed, and parametric study performed to identify the factors contributing to performance loss. The practical issues and challenges associated with the use of liquid metal for microfluidic tuning are addressed and dealt with.

The switch demonstrated an insertion loss of better than 0.5 dB and an average isolation of better than 15 dB for the K-band and better than 20 dB for 21 GHz-25 GHz range. The temperature effects on the performance of the switch were also studied for open and closed loop pumping configuration. The RF and the switch performance was found to be stable with a closed loop fluidic pumping.

5 Electroplated 3D printed waveguide and its application as a microfluidically controlled Single-Pole Double-Throw (SPDT) switch

In this chapter, another approach was taken for the metallization of the 3D printed thermoplastic waveguide structure to achieve functionality. Chapter 3 describes the use of conductive silver ink as the final conductive metal layer for the functional waveguide. Here, the alternate approach involves the use of ink only as a seed layer, onto which, a copper layer is deposited through the process of Electroplating. The copper plated waveguide is fabricated and it's RF performance compared with ink coated waveguide. Additionally, the microfluidically controlled switch concept developed in Chapter 4 is extended to develop a Single-Pole Double-Throw (SPDT) switch.

5.1 Electroplating Procedure

Electroplating is the application of a metal coating to a metallic or other conducting surface by an electrochemical process. The object to be plated, commonly called the workpiece, is made the cathode (negative electrode) of an electrolysis cell through which a direct electric current is passed. For the electrolysis to take place the workpiece to be plated needs to be conductive and our 3D printed waveguide (workpiece) structure is made of non-conductive thermoplastic. Hence, a seed layer needs to be brushed onto the surface of the structure responsible for functionality. Here, there conductive silver ink is used as a seed layer coating for the thermoplastic waveguide structure. The high viscosity adds the advantage of improving the surface roughness by adding a smoother layer on the surface.

Following the ink coating and drying of the 3D printed waveguide, it is immersed in an aqueous copper electroplating solution (the bath) containing a mixture of DI water, sulfuric acid, Copper (II) sulfate Pentahydrate, Polyethylene Glycol 3350 and a trace of hydrochloric acid. A plating current of 200mA was

applied to the solution for duration of 1 hour. The anode is usually a bar of the metal being plated. When the electric current is passed through the solution, by connecting the positive terminal of the battery to the anode and negative terminal to the cathode, the Copper ions from the solution go towards the cathode and get deposited on the work piece and form a thin anode goes on dissolving in the solution and finally gets deposited onto the work piece. Fig. 5-1 shows the final waveguide product after electroplating. It should be noted the discolouration of the copper layer is due to oxidation of copper. It should also be noted that for this procedure, thermoplastic waveguide structure is printed as a block instead of a having an overhanging flange and supports to build the flange as shown in Fig. 3-3. A solid block structure helps achieve a flatter flange, whereas the supported overhanging flanges resulted in slightly uneven flange surface. Printing a block instead of the branch-like support materials also reduces print time significantly.

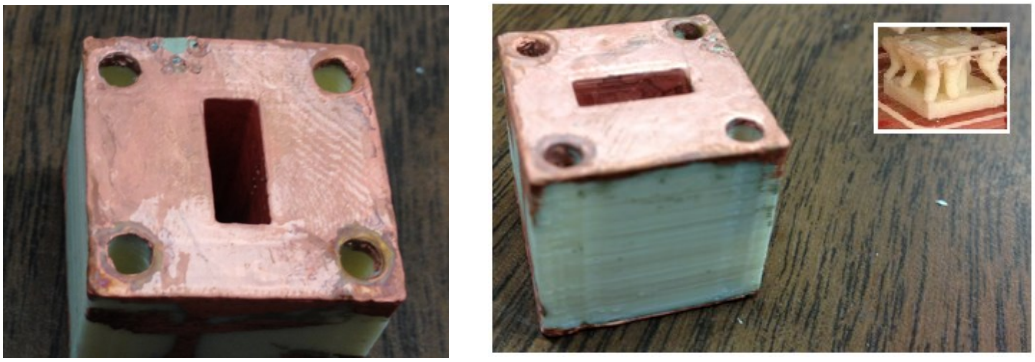

Fig. 5-1 Electroplated 3D printed waveguide.

5.2 RF Performance

5.2.1 Waveguide Performance

The measured performance of a 1cm solid block of ink coated waveguide before and after electroplating is plotted in Fig. 5-2. The plot shows an average return loss better than 25 dB in the frequency range 15-26.5 GHz. The insertion loss for the two lengths of waveguide before and after copper plating has been zoomed in,

and plotted in Fig. 5-3. The 1cm waveguide coated with a layer of ink demonstrates an insertion loss of less than 0.32 dB for the entire band. After electroplating the ink coated waveguide, the insertion loss is observed to have been improved to an average of 0.15 dB for the entire K-Band, for the 1cm waveguide. As expected, for the 2cm long waveguide, the insertion loss for both the ink coated and copper plated waveguide is observed to be higher. It should be noted that the increase in insertion loss is observed to be much lower for the copper plated waveguide, owing to higher conductivity of copper versus the conductive ink. The smoothened curves of the simulated and measured Insertion Loss for the 1cm 3D printed Copper plated waveguide is presented in in Fig. 5-4. The discrepancy between the simulation and measurements could be attributed to flange contacts, non-uniform metal coating and geometrical flaws.

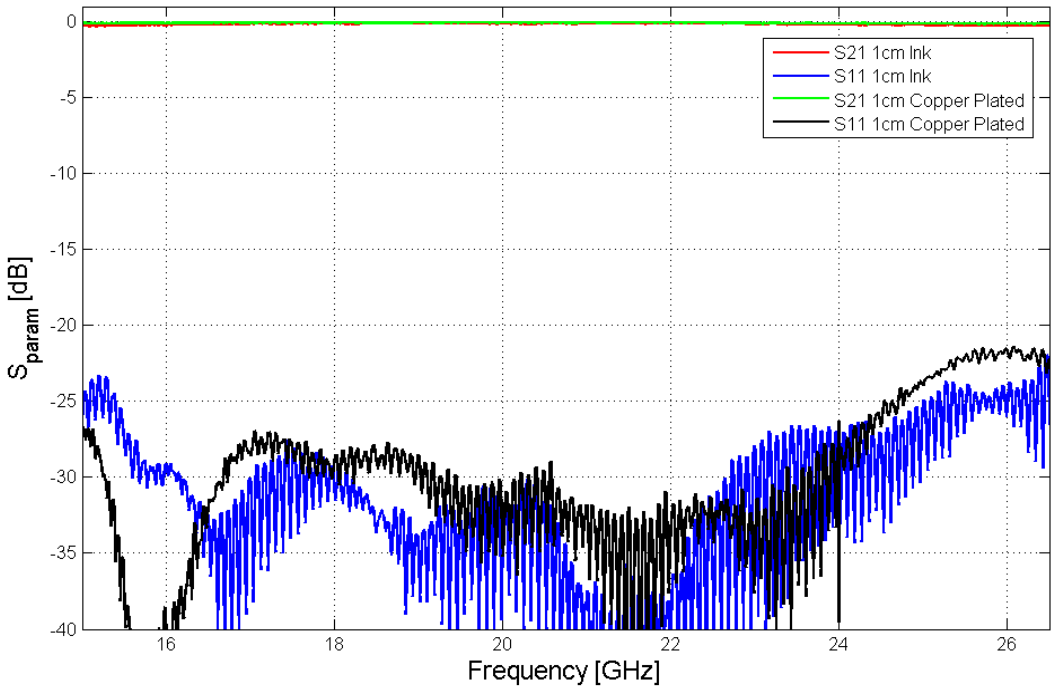

Fig. 5-2 Measured S-Parameter of Ink Coated Vs Copper Plated 3D printed Waveguide

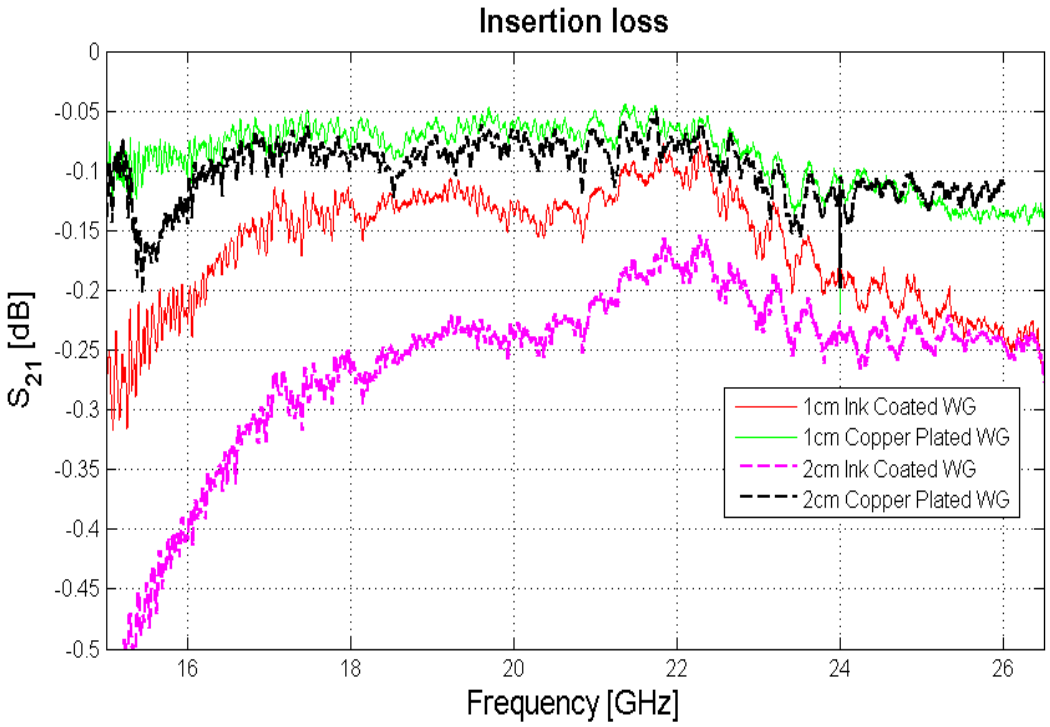

Fig. 5-3 Measured insertion loss for comparison for copper plated and ink coated 3D printed waveguides for 1cm and 2cm long WG lines.

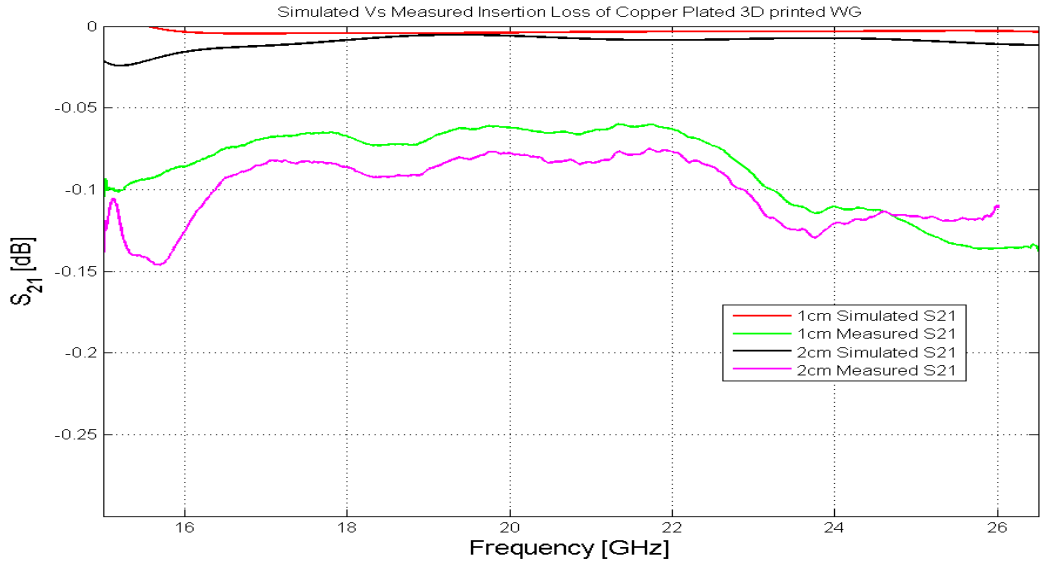

Fig. 5-4 Simulated and Measured Insertion Loss for a 1cm long 3D printed Copper plated waveguide.

To characterize the performance of the 3D printed waveguide and determine its attenuation (α) and propagation constant (β), a multiline method [70], [71] is performed, as detailed in Appendix B. The two lengths of waveguides were measured and their S-Parameters were used to extract the losses. Fig. 5-5 presents the attenuation and phase constants of the ink waveguide extracted from the simulated and measured S-parameters of two lengths of waveguide. Fig. 5-6 shows a zoomed in plot of the attention (a) and phase constant (b) for the copper plated waveguides. Comparing the extracted loss Fig. 5-5 for electroplated waveguides with that of ink coated waveguides in Fig. 3 8, it is evident that the average loss is much lower for the electroplated waveguides, for the entire K-band.

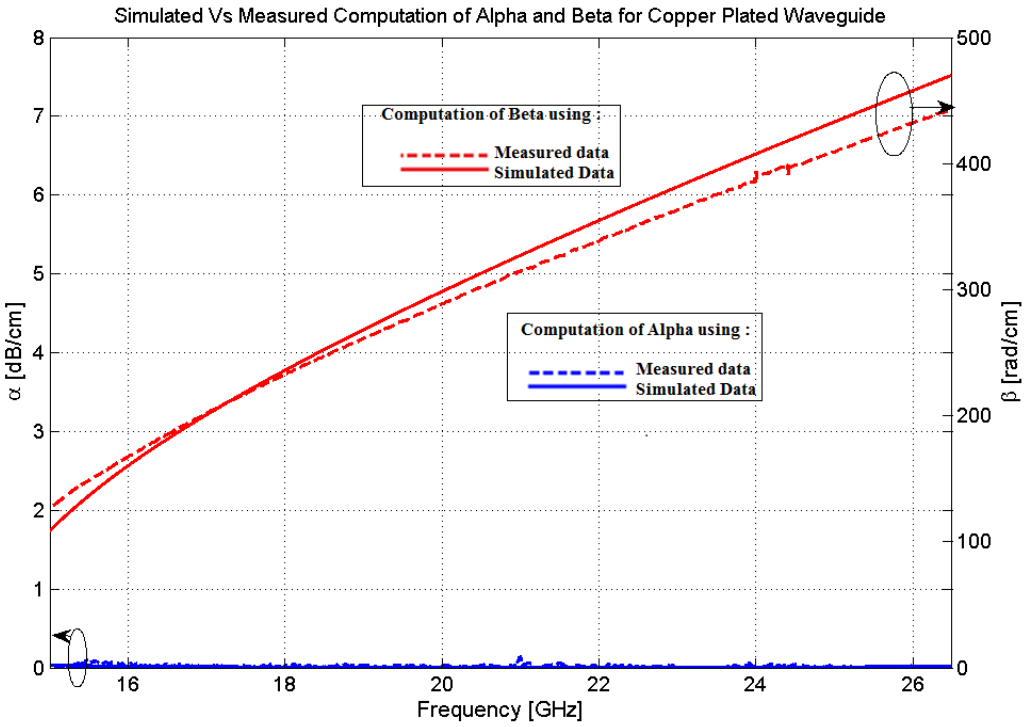

Fig. 5-5 Attenuation constant (α) and phase constant (β) calculated from two lengths of Electroplated 3D printed waveguides using simulated and measured S-Parameters.

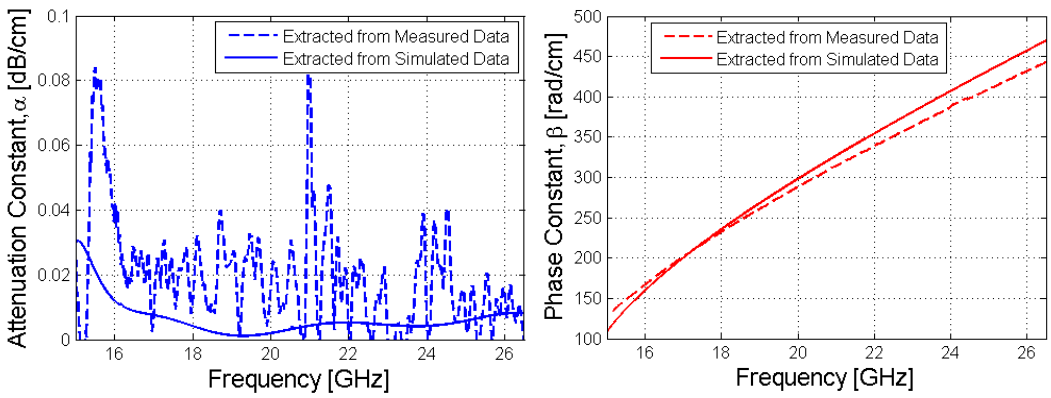

Fig. 5-6 Zoomed Plot of (a) Attenuation Constant and (b) Phase Constant

5.3 Surface Profiling

An Alpha-Step IQ surface profiler [93] was used to measure layer thickness and surface roughness before and after ink coating and copper plating a flat piece of 3D Printed ABS. The Alpha-step meter has a resolution of 0.1µm and is capable of measuring upto a step height of 2mm. A scan length of 2000µm is used with a scan speed of 50 µm/s and sampling rate of 500 Hz. A flat piece of sample divided into three sections (A, B and C) was used for the measurements, as shown in Fig. 5-7

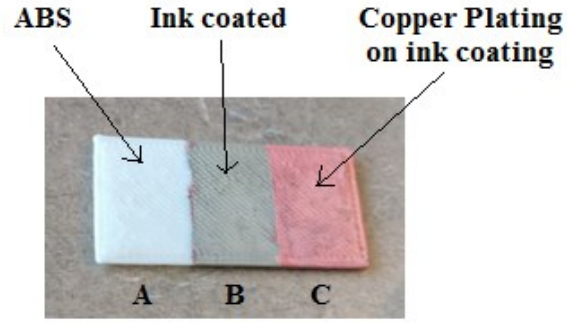

Fig. 5-7 Sample 3D printed sheet used for surface analysis shows sections of bare ABS (A), Ink coated ABS (B) and Copper plated (C).

Step height measurement:

For the step height measurement, the stylus of the profiler was dragged across the two layer steps. The first step was due the electroplated and ink coated junction

(Step 1) and the second step was ink coating to the bare ABS junction (Step 2) as shown in Fig. 5-8 (a).

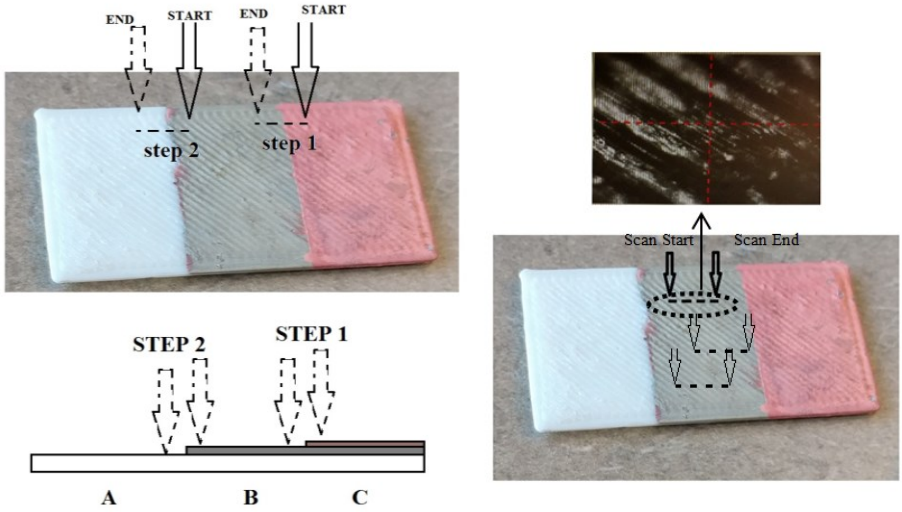

(a) (b)

Fig. 5-8 (a) Step height measurement (b) Surface line scan

For each of the two steps C to B and B to A, three readings were taken at three different locations and the average was noted. An average of 14.4 μm (~0.014mm) was recorded for the step height C to B, depicting the copper plated layer thickness. The average step height for the step B to A was measured to be 244 μm (~0.2mm).

Surface Line Scan:

Following this, a surface line scan was carried out using the Alpha-Step IQ surface profiler. For this measurement, the stylus was dragged across an area of each section of the sample, as shown in Fig. 5-8(b). From the obtained surface scan, the difference between the highest and the lowest peaks were recorded as the maximum roughness across the 2000μm scan length. To obtain a more reliable reading, three measurements were taken at different locations of each portion and an average of the readings was computed to note the maximum surface roughness of each sections.

Section A (Bare ABS): The surface line scan for the bare ABS section is shown in Fig. 5-9. From the scan readings measured at three different locations, the

average difference of maximum and minimum surface heights was found to be 153.7µm.

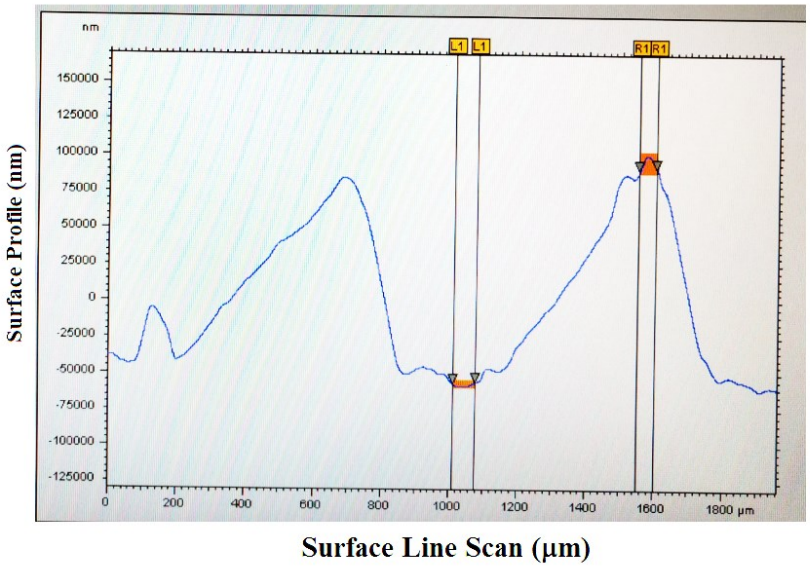

Fig. 5-9 Surface Line Scan for Bare ABS section (A).

Section B (Ink Coated): The surface line scan for the ink coated section is shown in Fig. 5-10. From the scan readings measured at three different locations, the average difference of maximum and minimum surface heights was found to be 34.15 µm.

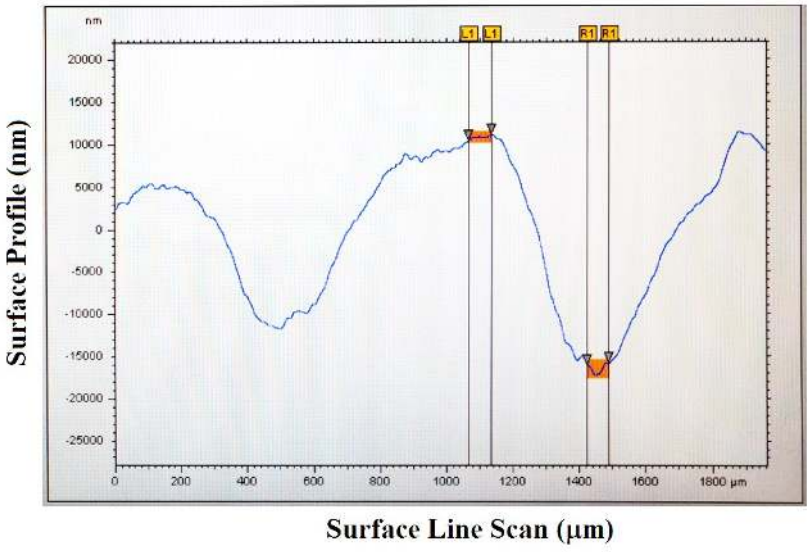

Fig. 5-10 Line Scan for Ink coated section (B).

Section C (Copper plated):

The surface line scan for the copper plated section is shown in Fig. 5-11. From the scan readings measured at three different locations, the average difference of maximum and minimum surface heights was found to be 23.02 μm.

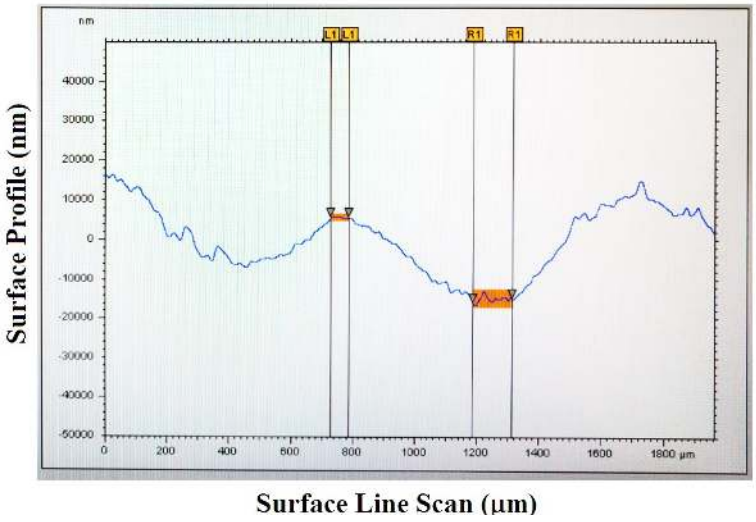

Fig. 5-11 Surface Line Scan for the Copper plated section (B).

The surface profile measurements are tabulated in Table 5-1. It is observed that the maximum surface roughness was obtained for the bare ABS section, while the ink coating reduced the roughness by more than 4 times. Hence, if can be concluded that the surface roughness can be majorly accounted for by the print resolution of the ABS lines. The high viscosity of the ink helps smoothen the surface to certain extent.

Table 5-1 SUMMARY OF SURFACE PROFILE

Surface	Layer thickness (μm)	Maximum Roughness (μm)
Section A (Bare ABS)	-	153.7
Section B (Ink Coated)	244	34.15
Section C (Copper plated)	14.4	23.02

5.4 Single-Pole Double-Throw (SPDT) Switch

Switch Model:

An SPDT switch comprises of one common port, and two other branching ports between which transmission path is switched. The three port structure is modelled in HFSS, as shown in Fig. 5-12, where port 1 is the input port, branching out into two output ports. The switching is done using the concept developed in Chapter 4. A set of 3 three tubes, containing Hydrocal 2400 as carrier liquid is inserted into each channel side, making a total of 6 tubes inserted into the device. For the ON State , the tubes are filled with oil to allow wave propagation, while for the OFF State , liquid metal plugs are pumped into the channels to create hindrance to the propagating waves. This is portrayed in Fig. 5-12 which shows the configuration for Port 3 to be in the ON State .

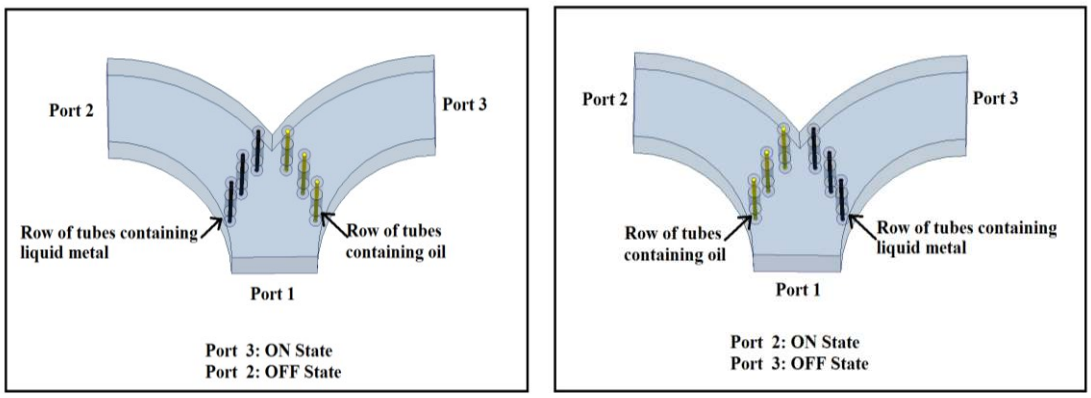

(a) (b)

Fig. 5-12 SPDT Switch Model.

Fabrication Process:

The first step of the fabrication process involves designing the CAD model of the SPDT structure in a way that is can be printed with the 3D printer with ease. The addition of overhanging flanges makes the structure particularly difficult to print as it

is. Hence, support structures were added to the design, as shown in green in Fig. 5-13(a). Fig. 5-13(b) shows the final product, 3D printed with ABS.

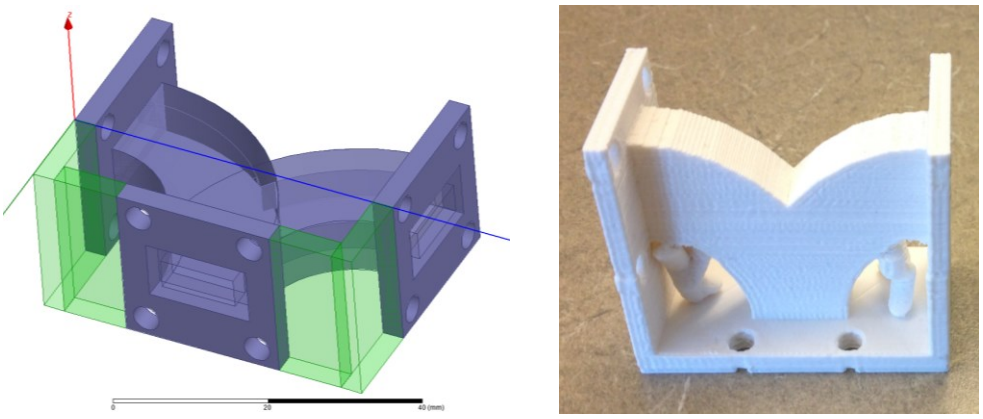

(a) (b)

Fig. 5-13 SPDT structure (a) Designed CAD model (b) Printed

Following this, the structure was brushed with conductive ink, AG 610 to activate the internal channel and the flanges for electroplating. The SPDT structure was then copper plated, using the electroplating setup and process depicted in Section 5.2. The final copper plated structure is displayed in Fig. 5-14. Holes were drilled into the structure to insert the oil and liquid metal carrying Teflon tubes.

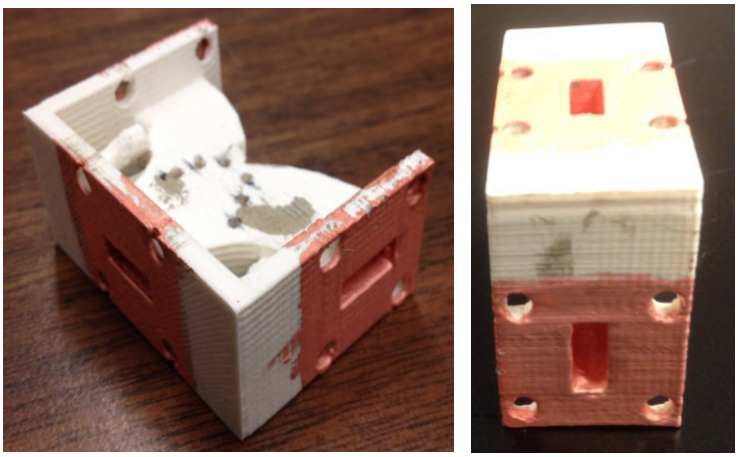

Fig. 5-14 SPDT Structure after Copper Plating.

5.4.1 SPDT Switch Performance

For the RF performance measurement, two test head coax to waveguide adaptors were connected to the input port and one output port at a time. Liquid metal is pumped through tubes to prevent wave propagation to the isolated port. To prevent mismatch and radiation losses, the isolated port is matched with a short. Ideally, the isolated port should be connected to another test head. Fig. 5-15 shows the switch assembly and measurement setup with two waveguide adapters that connect to a VNA for measurements. For the measurement, port 2 was set as the ON Port, and port 3 was set as the isolated port. Fig. 5-16 displays the measured ON State performance, when Port 2 is on.

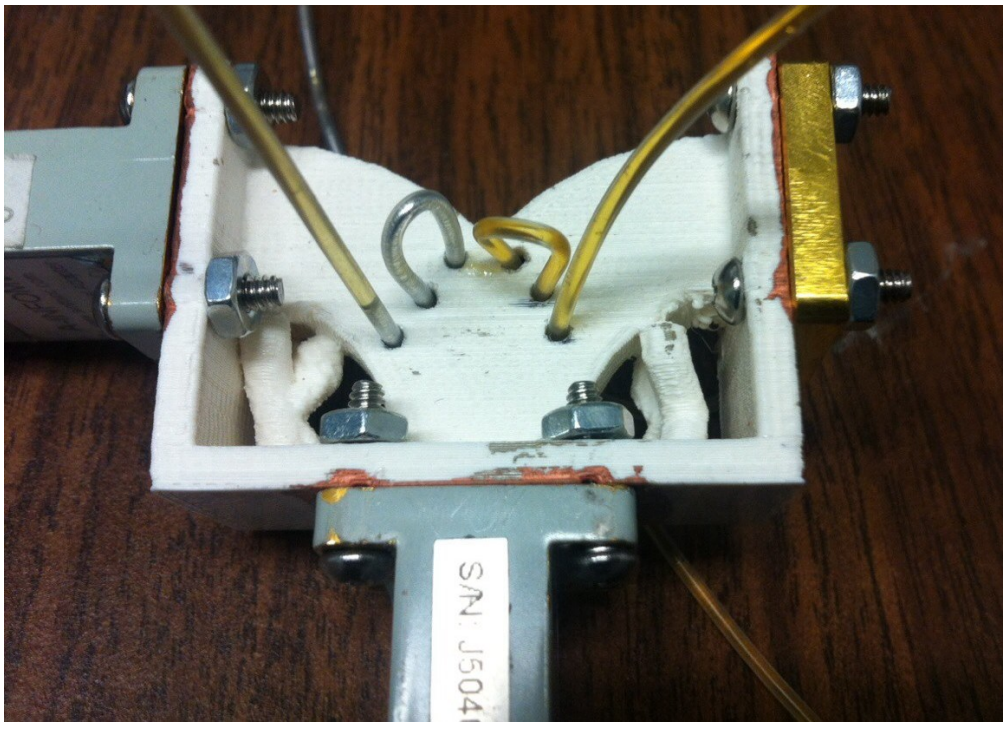

Fig. 5-15 SPDT switch with microfluidic tubes, connected to test heads for measurement.

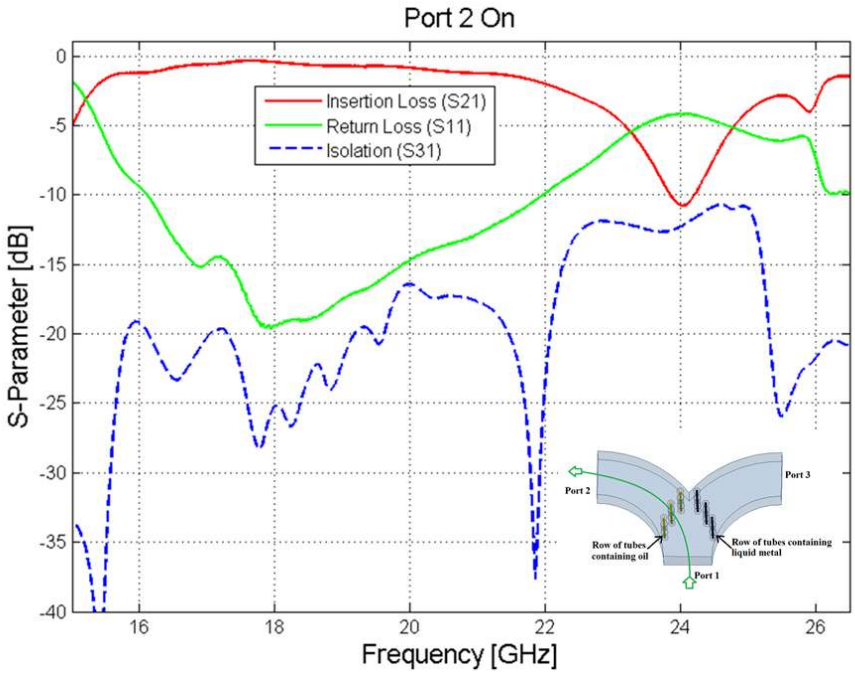

Fig. 5-16 Measured RF Performance of the SPDT Switch when Port 3 is ON

5.5 Summary and Discussion

This chapter introduces an Electroplated 3D printed plastic waveguides described in Section 3.1.1. Copper plated waveguides were fabricated and its RF performance compared with ink coated waveguides. RF measurements of the copper plated 3D printed waveguides reveal that the insertion loss is much better i.e. less than 0.15 dB for the entire band, compared to ink coated ones. The surface roughness is also characterized. It is illustrated that the surface roughness is improved by adding ink as adhesion layer and followed by electroplating.

With the electroplating process of metallization, it is possible to metallize even more complex structures. To demonstrate this, a Single-Pole Double-Throw waveguide switch structure is fabricated by 3D printing followed by electroplating. The switching is performed by microfluidically controlled liquid metal, utilizing the switch concept developed in Chapter 4. The preliminary results for the RF performance of the switch are presented in this chapter, leaving further scope of improvement by optimizing the position of the tubes.

6 Conclusion and Future Work

6.1 Summary and Conclusion

The main objective of this thesis was to investigate the potential of 3D printing manufacturing technology to fabricate functional RF devices. Aiming to achieve this goal, a K-Band hollow rectangular waveguide was fabricated using full 3D printing technology. The 3D printing process involves Fused Deposition Modelling (FDM) technique for plastic extrusion and ink dispensing technique to coat the non-conductive plastic structure with conductive ink that adds functionality to the structure. The fabricated 3D printed waveguide was characterized and its attenuation and propagation constants are computed for the K-Band using a multi-line technique. The measured RF performance is compared with high frequency structure simulation, and presented in Section 3.2. The discrepancy between the simulated and measured RF performance can be attributed to surface roughness, flange contacts and metal-ink conductivity, which can be improved by adopting high-end 3D printers and conductive ink.

Thus, the 3D fabricating technology used for the fabrication of hollow metallic waveguides enables low-cost, light-weight and rapid fabrication compared to the labor-intensive, time-consuming, expensive and complex conventional machining techniques. Furthermore, it helps meet the localized on-demand fabrication needs for RF device manufacturing and allows quick prototyping to perform necessary design iterations. This study shows the great potential and possibility for adapting 3D printing manufacturing technology.

Another research objective of this thesis was to explore the scope of microfluidic-based tuning in RF devices. To achieve this, a conceptual model of liquid metal actuation-based reflective waveguide switch was developed and implemented in the fabricated 3D printed waveguide. The liquid metal used in this work, Eutectic Gallium-Indium (EGaIn), is microfluidically controlled to attain a short circuit in the critical path of the incident RF signal. Thus, addition of liquid

metal posts inside the waveguide channels perturbs the field propagation within the waveguide, enabling ON and OFF States within the device.

The challenges associated with the use of liquid metal, such as surface oxidation leaving residues, and manipulation through channels, have been addressed and dealt with. Additional HFSS simulations performed with parametric study was performed to understand the effect of the fluids in use and channels on the switch performance, as outlined in Section 4.2. Generally, the results obtained in simulations and measurements are consistent. The insertion loss and isolation of the switch are measured to be better than 0.5 dB and better than 15 dB for the entire K-Band, respectively. Furthermore, the switch's performance with respect to changes in ambient temperature has been studied. The switching limitations are attributed to actuation mechanism for speed, and type of carrier fluid, tubes and for its RF performance.

In an attempt to improve the performance of the 3D printed waveguides and waveguide devices, the printed and ink coated waveguides were electroplated with copper. The higher conductivity of copper improved the waveguide RF performance significantly. Additionally, the switching concept was expanded to a Single-Pole Double-Throw which was also fabricated with 3D printing followed by copper plating. Preliminary measurements of the SPDT switch serves as proof of concept, leaving scope for much better performance with optimized location of tubes, improving consistency in device fabrication, and using low-loss tubes and carrier liquid.

Overall, the thesis successfully demonstrated the fabrication of functional waveguides and waveguide switches, using 3D printing manufacturing technology, incorporated with microfluidic tuning, offering overall ease of fabrication with good RF performance.

6.2 Future Study

The thesis proved the initial concept of using 3D printing to fabricate hollow metallic waveguide operating in the K-Band, and its application as a microfluidically controlled waveguide switch. The research that has been undertaken for this thesis has highlighted a number of topics on which further research would be beneficial to broaden the scope of 3D printing electronics and microfluidic-based tuning. Some potential areas to embark upon are:

Future Research for 3D Printing Technology:

- RF devices, being prone to losses as high frequencies, are sensitive to surface roughness and uniformity. These are limited by the printer resolution and extrusion tip size. Printing resolution, precision, and alignment play an important role in making this fabricating technology effective, for better fabrication tolerances. High resolution printers, although commercially available recently [83], tend to be expensive, and efforts need to be made reduce to the cost of such high-end machines.
- Speed of printing will depend on the speed at which the printer-head can extrude the raw material used. Hence the production time depends on the number of layers printed, which can last for hours or days, limiting the technology only for prototyping and not for 'mass-production'.
- Research in the build of 3D printers and materials, that enable simultaneous and continuous 5-axis extrusion of ink and plastic would aid tremendously.. Currently, the dual extrusion systems available suffer from the challenge of preventing the conductive ink from drying up due to the heat of the FDM extrusion head in the chamber.
- Additionally, Research oriented particularly towards both the FDM printing materials and conductive ink would be profoundly beneficial. Advent of stronger printing materials with higher stability to temperate would potentially improve the scope of such 3D printed devices. Additionally, the use of

conductive nano-particle ink with higher conductivity would increase the RF performance of such ink-coated 3d printed devices significantly. Another material drawback that needs attention is that Layer by layer build-up leads to a structural weakness in the 3rd (vertical) dimension.

- An interesting research area is the development of conductive polymers for FDM extrusion, which currently suffers from the drawback of low conductivity.

3D printing Waveguide and Microfluidic Switches:

- The 3D printed waveguide suffered from the drawback of surface roughness. High resolution printers could potentially improve the surface roughness. Use of narrower extrusion tips and ink with lower particle size could potentially improve the surface roughness.
- Ink Characterization and research focused on the development of ink compositions to acquire high conductivity, with low curing needs and offer ease of use would be highly beneficial.
- Study on the surface roughness of the conductive layer of ink and its effect of the RF performance is another area of interest.
- For the overflow technique, the use of ink with lower surface tension could potentially improve the coating process. Additionally, to improve the uniformity in ink coating, research focused towards developing techniques to coat narrow channels would be beneficial to take this study further. Printers offering simultaneous ink and plastic printing options could help achieve the goal.
- Although the basic operation of the switches is confirmed, the reliability and lifetime study has not been performed. The use of fluids does raise some concerns for certain applications and hence it needs to be studied further.
- Although this work uses micropumps for the fluidic section, utilization of the recently introduced electro-capillary actuation of liquid metals would be an intriguing research area.

- The power handling of the waveguide and the switch are yet to be determined leaving scope for further study.
- The most important practical concerns regarding liquid metal based tuning are the liquid metal residues due to oxidization, switching speed and precise position control. Characterization of switching speed, and RF performance, different actuation mechanisms and carrier fluids could potentially improve this research further.

7 References

[1] Appen T. Srivatsan and T. Sudarshan, *Additive manufacturing*. Taylor & Francis, 2015.

[2] B. H. Lipson, “3D Printing , Now and Beyond 3D Printing , Now and Beyond.” Stratasys White Paper, Jun 23 2016.

[3] J. P. Kruth, “Material Incress Manufacturing by Rapid Prototyping Techniques,” *CIRP Annals - Manufacuring Technology*, vol. 40, no. 2, pp. 603–614, 1991.

[4] D.T Pham and R.S Gault, “A comparison of rapid prototyping technologies,” *International Journal of Machine Tools and Manufacture*, vol. 38, no. 10–11, pp. 1257–1287, 1998.

[5] E. Macdonald *et al*., "3D Printing for the Rapid Prototyping of Structural Electronics," in *IEEE Access*, vol. 2, no. , pp. 234-242, Dec. 2014.

[6] B. Zhang *et al*., "Metallic 3-D Printed Antennas for Millimeter- and Submillimeter Wave Applications," in *IEEE Transactions on Terahertz Science and Technology*, vol. 6, no. 4, pp. 592-600, July 2016.

[7] Huang Guan-Long, Zhou Shi-Gang, Chio Tan-Huat and Yeo Tat-Soon, "3-D metal-direct-printed wideband and high-efficiency waveguide-fed antenna array," 2015 IEEE MTT-S International Microwave Symposium, Phoenix, AZ, 2015, pp. 1-4.

[8] B. Zhang and H. Zirath, "A Metallic 3-D Printed E-Band Radio Front End," in *IEEE Microwave and Wireless Components Letters*, vol. 26, no. 5, pp. 331-333, May 2016.

[9] B. Zhang and H. Zirath, "Metallic 3-D Printed Rectangular Waveguides for Millimeter-Wave Applications," in *IEEE Transactions on Components, Packaging and Manufacturing Technology*, vol. 6, no. 5, pp. 796-804, May 2016.

[10] B. Zhang and H. Zirath, "3D printed iris bandpass filters for millimetre-wave applications," in *Electronics Letters*, vol. 51, no. 22, pp. 1791-1793, 10 22 2015.

[11] E. A. Rojas-Nastrucci, J. Nussbaum, T. M. Weller and N. B. Crane, "Meshed rectangular waveguide for high power, low loss and reduced weight applications," *2016 IEEE MTT-S International Microwave Symposium (IMS)*, San Francisco, CA, 2016, pp. 1-4.

[12] N. T. Nguyen, N. Delhote, M. Ettorre, D. Baillargeat, L. Le Coq and R. Sauleau, "Design and Characterization of 60-GHz Integrated Lens Antennas Fabricated Through Ceramic Stereolithography," in *IEEE Transactions on Antennas and Propagation*, vol. 58, no. 8, pp. 2757-2762, Aug. 2010.

[13] B. Sanz-Izquierdo and E. A. Parker, "3-D Printing of Elements in Frequency Selective Arrays," in *IEEE Transactions on Antennas and Propagation*, vol. 62, no. 12, pp. 6060-6066, Dec. 2014.

[14] P. Nayeri *et al*., "3D Printed Dielectric Reflectarrays: Low-Cost High-Gain Antennas at Sub-Millimeter Waves," in *IEEE Transactions on Antennas and Propagation*, vol. 62, no. 4, pp. 2000-2008, April 2014.

[15] K. Gbele, M. Liang, W. R. Ng, M. E. Gehm and H. Xin, "Millimeter wave luneburg lens antenna fabricated by polymer jetting rapid prototyping,"*2014 39th International Conference on Infrared, Millimeter, and Terahertz waves (IRMMW-THz)*, Tucson, AZ, 2014, pp. 1-1.

[16] J. C. S. Chieh, B. Dick, S. Loui and J. D. Rockway, "Development of a Ku-Band Corrugated Conical Horn Using 3-D Print Technology," in *IEEE Antennas and Wireless Propagation Letters*, vol. 13, pp. 201-204, 2014.

[17] M. Mirzaee, S. Noghanian, L. Wiest and I. Chang, "Developing flexible 3D printed antenna using conductive ABS materials," *2015 IEEE International Symposium on Antennas and Propagation & USNC/URSI National Radio Science Meeting*, Vancouver, BC, 2015, pp. 1308-1309.

[18] M. Ahmadloo and P. Mousavi, "A novel integrated dielectric-and-conductive ink 3D printing technique for fabrication of microwave devices," *Microwave Symposium Digest (IMS), 2013 IEEE MTT-S International*, Seattle, WA, 2013, pp. 1-3.

[19] M. Ahmadloo and P. Mousavi, "Application of novel integrated dielectric and conductive ink 3D printing technique for fabrication of conical spiral

antennas," *2013 IEEE Antennas and Propagation Society International Symposium (APSURSI)*, Orlando, FL, 2013, pp. 780-781.

[20] Adams, J. J., Duoss, E. B., Malkowski, T. F., Motala, M. J., Ahn, B. Y., Nuzzo, R. G., Bernhard, J. T. and Lewis, J. A. (2011), "Conformal Printing of Electrically Small Antennas on Three-Dimensional Surfaces," *Advanced Materials*, vol.23, issue 11, pp.1335–1340, 2011.

[21] S. Mufti, A. Tennant and L. Seed, "3D electrically small dome antenna," *Antennas and Propagation Conference (LAPC), 2014 Loughborough*, Loughborough, 2014, pp. 653-656.

[22] J. Kimionis, A. Georgiadis, M. Isakov, H. J. Qi and M. M. Tentzeris, "3D/inkjet-printed origami antennas for multi-direction RF harvesting,"*2015 IEEE MTT-S International Microwave Symposium*, Phoenix, AZ, 2015, pp. 1-4.

[23] N. Arnal *et al*., "3D multi-layer additive manufacturing of a 2.45 GHz RF front end," *2015 IEEE MTT-S International Microwave Symposium*, Phoenix, AZ, 2015, pp. 1-4.

[24] S. Javidmehr,"3D-Printed Microstrip Resonators for 4.7T MRI," M.S. Thesis, University of Alberta, Canada, 2015.

[25] M. D'Auria *et al*., "3-D Printed Metal-Pipe Rectangular Waveguides," in *IEEE Transactions on Components, Packaging and Manufacturing Technology*, vol. 5, no. 9, pp. 1339-1349, Sept. 2015.

[26] E. G. Geterud, P. Bergmark and J. Yang, "Lightweight waveguide and antenna components using plating on plastics," *Antennas and Propagation (EuCAP), 2013 7th European Conference on*, Gothenburg, 2013, pp. 1812-1815.

[27] M. I. M. Ghazali, E. Gutierrez, J. C. Myers, A. Kaur, B. Wright and P. Chahal, "Affordable 3D printed microwave antennas," *2015 IEEE 65th Electronic Components and Technology Conference (ECTC)*, San Diego, CA, 2015, pp. 240-246.

[28] G. P. Le Sage, "3D Printed Waveguide Slot Array Antennas," in *IEEE Access*, vol. 4, no. , pp. 1258-1265, 2016.

[29] R. Zhu and D. Marks, "Rapid prototyping lightweight millimeter wave antenna

and waveguide with copper plating," *2015 40th International Conference on Infrared, Millimeter, and Terahertz waves (IRMMW-THz)*, Hong Kong, 2015, pp. 1-2.

[30] M. Liang, C. Shemelya, E. MacDonald, R. Wicker and H. Xin, "3-D Printed Microwave Patch Antenna via Fused Deposition Method and Ultrasonic Wire Mesh Embedding Technique," in *IEEE Antennas and Wireless Propagation Letters*, vol. 14, no. , pp. 1346-1349, 2015.

[31] L. Min, X. Yu, C. Shemelya, E. MacDonald, and X. Hao, "3-D printed multilayer microstrip line structure with vertical transition toward integrated systems," *in Proc. IEEE MTT-S International Microwave Symposium* (IMS), 2015, pp. 1–4.

[32] P. I. Deffenbaugh, T. M. Weller and K. H. Church, "Fabrication and Microwave Characterization of 3-D Printed Transmission Lines," in *IEEE Microwave and Wireless Components Letters*, vol. 25, no. 12, pp. 823-825, Dec. 2015.

[33] D. Pozar, *Microwave engineering*. Hoboken, NJ: Wiley, 2012.

[34] Averse, "Diplexer1", Wikipedia. [Online]. Available: https://commons.wikimedia.org/wiki/File:Diplexer1.jpg# [Accessed: 03- Sep- 2016].

[35] Huawei, "5G : A Technology Vision," *Huawei, White paper*, pp. 1–16, 2014.

[36] "Waveguide collection", Wikipedia. [Online]. Available: https://commons.wikimedia.org/wiki/File:Waveguide_collection.jpg# [Accessed: 03- Sep- 2016].

[37] S. Adam, *Microwave theory and applications*. Englewood Cliffs, N.J.: Prentice-Hall, 1970.

[38] A. Horn III, J.W. Reynolds, P.A. LaFrance, and J.C. Rautio, 'Effect of conductor profile on the insertion loss, phase constant, and dispersion in thin high frequency transmission lines," in *DesignCon* 2010, 2010.

[39] S.P. Morgan Jr., "Effect of Surface Roughness on Eddy Current Losses at Microwave Frequencies," Journal of Applied Physics, Vol. 20, p. 352-362, April, 1949.

[40] L.B. Simonovich, “Practical Conductor Roughness Modeling with Cannonballs,”

White paper, no. 2, 2015.

[41] X. Ma, “Modeling of Conductor Surface Roughness Effect,” M.Sc. Thesis, University

of Illinois, Illinois, 2014.

[42] P. G. Huray *et al*., "Fundamentals of a 3-D “snowball” model for surface roughness power losses," *Signal Propagation on Interconnects, 2007. SPI 2007. IEEE Workshop on*, Genova, 2007, pp. 121-124...

[43] Leung Tsang, Xiaoxiong Gu and H. Braunisch, "Effects of random rough surface on absorption by conductors at microwave frequencies," in *IEEE Microwave and Wireless Components Letters*, vol. 16, no. 4, pp. 221-223, April 2006...

[44] R. Ding, L. Tsang and H. Braunisch, "Wave Propagation in a Randomly Rough Parallel-Plate Waveguide," in *IEEE Transactions on Microwave Theory and Techniques*, vol. 57, no. 5, pp. 1216-1223, May 2009.

[45] Y. Shlepnev and C. Nwachukwu, "Roughness characterization for interconnect analysis," *Electromagnetic Compatibility (EMC), 2011 IEEE International Symposium on*, Long Beach, CA, USA, 2011, pp. 518-523.

[46] C. E. Collins *et al*., "A new micro-machined millimeter-wave and terahertz snap-together rectangular waveguide technology," in *IEEE Microwave and Guided Wave Letters*, vol. 9, no. 2, pp. 63-65, Feb 1999.

[47] R. Zhu and D. Marks, "Rapid prototyping lightweight millimeter wave antenna and waveguide with copper plating," *2015 40th International Conference on Infrared, Millimeter, and Terahertz waves (IRMMW-THz)*, Hong Kong, 2015, pp. 1-2.

[48] Ant Nachrichtentechnik Gmbh, “Rotary Microwave Switch,” U.S. Patent 4649355, March, 10, 1987.

[49] D.-K. M. Corporation, "RF switch, Waveguide switches and Matrices - Dowkey microwave components," in *dowkey*. [Online]. Available:

http://www.dowkey.com/product_search.php. Accessed: Sep. 3, 2016.

[50] M. Sterner, N. Roxhed, G. Stemme and J. Oberhammer, "Static Zero-Power-Consumption Coplanar Waveguide Embedded DC-to-RF Metal-Contact MEMS Switches in Two-Port and Three-Port Configuration," in *IEEE Transactions on Electron Devices*, vol. 57, no. 7, pp. 1659-1669, July 2010.

[51] M. Daneshmand, and R. R. Mansour, "Multiport MEMS-Based Waveguide," *IEEE Transactions on Microwave Theory and Techniques*, vol. 53, no. 11, pp. 3531–3537, 2005.

[52] N. Vahabisani and M. Daneshmand, "Realization of a new class of monolithic RF MEMS waveguide switches for millimeter-wave applications," *2014 IEEE MTT-S International Microwave Symposium (IMS2014)*, Tampa, FL, 2014, pp. 1-4.

[53] N. Vahabisani and M. Daneshmand, "Study of Contact Resistance for Curled-Up Beams in Waveguide Switch," in *IEEE Microwave and Wireless Components Letters*, vol. 22, no. 11, pp. 586-588, Nov. 2012.

[54] R. F. Soohoo, "A Ferrite Cutoff Switch," in *IRE Transactions on Microwave Theory and Techniques*, vol. 7, no. 3, pp. 332-336, July 1959.

[55] T. Sickel, P. Meyer and P. W. van der Walt, "An in situ Tunable Diode Mounting Topology for High-Power X-Band Waveguide Switches," in *IEEE Transactions on Microwave Theory and Techniques*, vol. 55, no. 2, pp. 281-286, Feb. 2007.

[56] Chung-Hao Chen and D. Peroulis, "A Ka-band waveguide water-based absorptive switch with an integrated micropump," *Microwave Symposium Digest, 2008 IEEE MTT-S International*, Atlanta, GA, 2008, pp. 185-188.

[57] B. J. Lei, A. Zamora, T. F. Chun, A. T. Ohta and W. A. Shiroma, "A Wideband, Pressure-Driven, Liquid-Tunable Frequency Selective Surface," in *IEEE Microwave and Wireless Components Letters*, vol. 21, no. 9, pp. 465-467, Sept. 2011.

[58] Z. Wu, K. Hjort and S. H. Jeong, "Microfluidic Stretchable Radio-Frequency Devices," in *Proceedings of the IEEE*, vol. 103, no. 7, pp. 1211-1225, July 2015.

[59] C. H. Chen and D. Peroulis, "Liquid RF MEMS Wideband Reflective and Absorptive Switches," in *IEEE Transactions on Microwave Theory and Techniques*, vol. 55, no. 12, pp. 2919-2929, Dec. 2007.

[60] D. Rodrigo, L. Jofre and B. A. Cetiner, "Circular Beam-Steering Reconfigurable Antenna With Liquid Metal Parasitics," in *IEEE Transactions on Antennas and Propagation*, vol. 60, no. 4, pp. 1796-1802, April 2012.

[61] B. J. Lei, A. Zamora, T. F. Chun, A. T. Ohta and W. A. Shiroma, "A Wideband, Pressure-Driven, Liquid-Tunable Frequency Selective Surface," in *IEEE Microwave and Wireless Components Letters*, vol. 21, no. 9, pp. 465-467, Sept. 2011.

[62] A. Pourghorban Saghati, J. Singh Batra, J. Kameoka and K. Entesari, "A Microfluidically Reconfigurable Dual-Band Slot Antenna With a Frequency Coverage Ratio of 3:1," in *IEEE Antennas and Wireless Propagation Letters*, vol. 15, no. , pp. 122-125, 2016.

[63] A. P. Saghati, Sina Baghbani Kordmahale, J. Kameoka and K. Entesari, "A reconfigurable quarter-mode substrate integrated waveguide cavity filter employing liquid-metal capacitive loading," *2015 IEEE MTT-S International Microwave Symposium*, Phoenix, AZ, 2015, pp. 1-3.

[64] Shuyan Guo, Bao Jun Lei, Wenqi Hu, W. A. Shiroma and A. T. Ohta, "A tunable low-pass filter using a liquid-metal reconfigurable periodic defected ground structure," *Microwave Symposium Digest (MTT), 2012 IEEE MTT-S International*, Montreal, QC, Canada, 2012, pp. 1-3.

[65] M. Kelley *et al*., "Frequency reconfigurable patch antenna using liquid metal as switching mechanism," in *Electronics Letters*, vol. 49, no. 22, pp. 1370-1371, Oct. 24 2013.

[66] M. Wang, C. Trlica, M. R. Khan, M. D. Dickey, and J. J. Adams, "A reconfigurable liquid metal antenna driven by electrochemically controlled capillarity," *Journal of Applied Physics*, vol. 117, no. 19, 2015.

[67] M. U. Memon, K. Ling, Y. Seo, and S. Lim, "Frequency-switchable half-mode substrate-integrated waveguide antenna injecting eutectic gallium indium (EGaIn) liquid metal alloy," *Journal of Electromagnetic Waves and*

Applications, vol. 29, no. 16, pp. 2207–2215, 2015.

[68] M. U. Memon and S. Lim, "Effects of metallic caps for liquid metal in substrate integrated waveguide antenna," *2015 Asia-Pacific Microwave Conference (APMC)*, Nanjing, 2015, pp. 1-3.

[69] C. Koo, B. E. LeBlanc, M. Kelley, H. E. Fitzgerald, G. H. Huff and A. Han, "Manipulating Liquid Metal Droplets in Microfluidic Channels With Minimized Skin Residues Toward Tunable RF Applications," in *Journal of Microelectromechanical Systems*, vol. 24, no. 4, pp. 1069-1076, Aug. 2015.

[70] M. R. Khan, C. Trlica, J. So, M. Valeri, and M. D. Dickey, "Influence of water on the interfacial behavior of gallium liquid metal alloys," *ACS Applied Materials & Interfaces*, vol. 6, no. 24, pp. 22467–73, 2014.

[71] M. D. Dickey, R. C. Chiechi, R. J. Larsen, E. A. Weiss, D. A. Weitz, and G. M. Whitesides, "Eutectic Gallium-Indium (EGaIn): A Liquid Metal Alloy for the Formation of Stable Structures in Microchannels at Room Temperature," *Advanced Functional Materials*, vol. 18, no. 7, pp. 1097–1104, 2008.

[72] A. P. Saghati, J. Batra, J. Kameoka and K. Entesari, "Microfluidically-tuned miniaturized planar microwave resonators," *Wireless and Microwave Technology Conference (WAMICON), 2014 IEEE 15th Annual*, Tampa, FL, 2014, pp. 1-3.

[73] A. Dey, R. Guldiken and G. Mumcu, "Wideband frequency tunable liquid metal monopole antenna," *2013 IEEE Antennas and Propagation Society International Symposium (APSURSI)*, Orlando, FL, 2013, pp. 392-393.

[74] R. C. Gough, A. M. Morishita, J. H. Dang, M. R. Moorefield, W. A. Shiroma, and A. T. Ohta, "Rapid electrocapillary deformation of liquid metal with reversible shape retention," *Micro & Nano Systems Letters*, vol. 3, no. 4, pp. 1–9, 2015.

[75] S. Khan, N. Vahabisani and M. Daneshmand, "A Fully 3D Printed Waveguide and its Application as Microfluidically Controlled Waveguide Switch." IEEE Transactions on Components, Packaging and Manufacturing Technology, to be published.

[76] ANSYS, "ANSYS HFSS - High Frequency Electromagnetic Field

Simulation.” [Online]. Available: http://www.ansys.com/Products/Electronics/ANSYS-HFSS.

[77] A. Ranellucci, “Slic3r: Gcode generator for 3D printers,” 2015. [Online]. Available: http://slic3r.org/. Accessed: Sep. 3, 2016.

[78] Repetier, “ Repetier-Host.” [Online]. Available: http://www.repetier.com/. Accessed: Sep. 3, 2016.

[79] Machina, “Machina Corp – Desktop 3D Printers & Services.” [Online]. Available: http://www.machinacorp.ca/. Accessed: Sep. 3, 2016.

[80] By Priybrat (Microsoft Power Point) [GFDL (http://www.gnu.org/copyleft/fdl.html) or CC BY-SA 3.0 (http://creativecommons.org/licenses/by-sa/3.0)], via Wikimedia Commons. Accessed: Sep. 3, 2016.

[81] Autodesk, "Autodesk Meshmixer," in Meshmixer, 2016. [Online]. Available: http://meshmixer.com/. Accessed: Sep. 6, 2016.

[82] Conductive Compounds, “AG-610 Silver Conductive Ink.” [Online]. Available: http://www.conductivecompounds.com/silver-inks/ag-610-silver-conductive-ink.html. Accessed: Sep. 3, 2016.

[83] nScrypt, "Tabletop series," in *nScrypt*, 2015. [Online]. Available: http://nscrypt.com/3d-series-equipment/tabletop. Accessed: Sep. 3, 2016.

[84] "Cohesion and Adhesion in Liquids: Surface Tension and Capillary Action," in *OpenStax CNX*. [Online]. Available: https://cnx.org/contents/7vEquViP@4/Cohesion-and-Adhesion-in-Liqui. Accessed: Sep. 3, 2016.

[85] R. B. Marks, "A multiline method of network analyzer calibration," in *IEEE Transactions on Microwave Theory and Techniques*, vol. 39, no. 7, pp. 1205-1215, Jul 1991.

[86] A. M. Abbosh, "Analytical closed-form solutions for different configurations of parallel-coupled microstrip lines," in *IET Microwaves, Antennas & Propagation*, vol. 3, no. 1, pp. 137-147, February 2009.

[87] T. C. Company, "Fluoroplastic comparison - typical properties," in *Chemours*, 2013. [Online]. Available:

https://www.chemours.com/Teflon_Industrial/en_US/tech_info/techinfo_compare.html. Accessed: Sep. 3, 2016.

[88] Bartels Mikrotechnik, "Bartels Mikrotechnik GmbH - Micropumps," in *bartels-mikrotechnik*. [Online]. Available: http://www.bartels-mikrotechnik.de/content/view/9/15/lang,english/. Accessed: Sep. 3, 2016.

[89] Reed Instruments, "REED ST-8839 non-contact laser thermometer(discontinued) in Toronto, Canada," in *Reed Instruments*. [Online]. Available: http://www.reedinstruments.ca/laser-thermometers/reed-st-8839.html. Accessed: Sep. 3, 2016.

[90] Calumet, "Naphthenic base oils," in *Calumet Lubricants*, 2016. [Online]. Available: http://www.calumetlubricants.com/naphthenic-base-oils. Accessed: Sep. 3, 2016.

[91] T. C. Company, "Available grades of Chemours Teflon™ AF," in *Chemours*, 2016. [Online]. Available: https://chemours.com/Teflon_Industrial/en_US/products/product_by_name/teflon_af/grades.html. Accessed: Sep. 3, 2016.

[92] Y. A. Çengel, J. M. Cimbala, and Y. A. Cengel, *Fluid mechanics: Fundamentals and applications*, 3rd ed. New York, NY, United States: McGraw Hill Higher Education, 2013.

[93] KLA Tencor, "Surface Profilometry and surface Metrology," in *kla-tencor*, 2015. [Online]. Available: http://www.kla-tencor.com/surface-profilometry-and-metrology.html. Accessed: Sep. 3, 2016.

[94] N. Vahabisani, S. Khan, M. Daneshmand, "A K-Band Reflective Waveguide Switch Using Liquid Metal," submitted for publication.

[95] Vahabisani, "3D Micro-fabricated Millimeter-wave Devices: Waveguides and Waveguide Switches," Ph.D. Thesis, University of Alberta, Canada, 2014.

Appendix A

K-Band Reflective Waveguide Switch Using Liquid Metal

A.1 Implementation and Characterization

In Chapter 3, a microfluidically controlled reflective waveguide switch concept was developed and applied to the fabricated 3D printed waveguide. The switch concept is further applied on a commercially available hollow metallic waveguide and its RF performance characterized. The work presented in this Appendix has been submitted for publication [94].

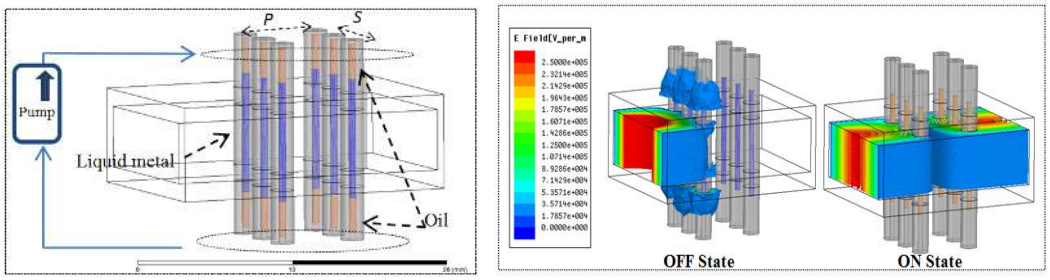

(a) (b)

Fig. A-1 Proposed microfluidic waveguide switch (a) Schematic Overview (b) Electric field distribution OFF State (liquid metal inserted) and ON State (liquid metal removed)

The general overview of the proposed K-band switch is presented in Fig A-1. As depicted in this figure, microfluidic channels connected to a micro-pump are inserted into a WR-42 waveguide along the broad-wall. It is anticipated that the number of microfluidic channels and their spacing also affects the switch performance. Considering the design and implementation requirements, only 3 holes per row are positioned along the waveguide broad wall. The optimized dimension and location of the tubes are listed in Table A-1, where R_O and R_i are the tube's outer and inner diameters respectively.

Table A-1: THE OPTIMIZED PARAMETERS OF THE SWITCH

Symbol	Value	Symbol	Value
R_O	1.60 mm	*S*	3.00 mm
R_i	0.50 mm	*P*	5.00 mm

The electric field distribution of the switch in both ON and OFF State is simulated using full mode ANSYS HFSS software and shown in Fig. A-2. The OFF state performance of the switch for 1 and 2 rows of microfluidic channels (3 tubes per row) is presented in Fig. A-2 (b). Evidently, as the number of the rows increases from 1 to 2, higher isolation is achieved.

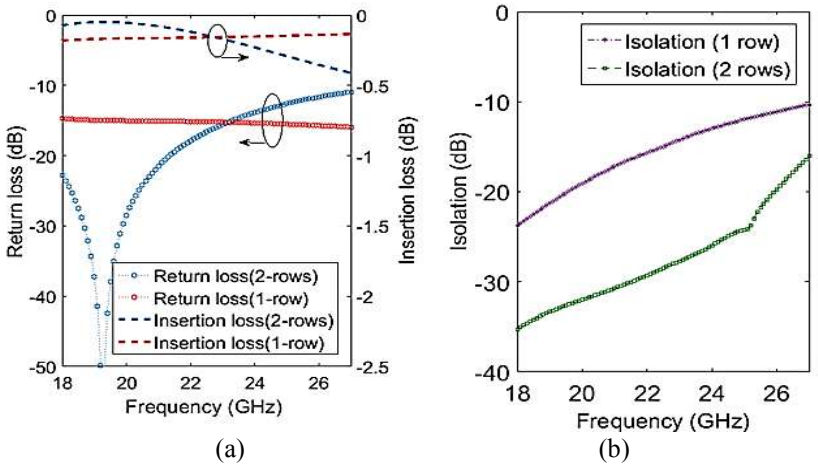

(a) (b)

Fig. A-2 The simulated RF performance of the proposed microfluidic switch, (a) ON State , and (b), OFF State

The implemented prototype of the switch is shown in Fig. A-3. To realize the switch, the appropriate size holes are drilled in the broad wall of the waveguide and PTFE tube is inserted. A syringe pump is then used to inject the EGaIn into the PTFE tubes, with Hydrocal 2400 oil as carrier liquid. To control the precise movement of the liquid metal, Bartel's piezoelectric Diaphragm micro-pump (mp6) is used in a closed-loop configuration. In the setup shown in Fig. A-3, the attached controller board enables the dynamic control of the flow rate. For the setup presented in this work, the speed was measured to be 0.73 mm/sec, with our choice of tube and oil carrier

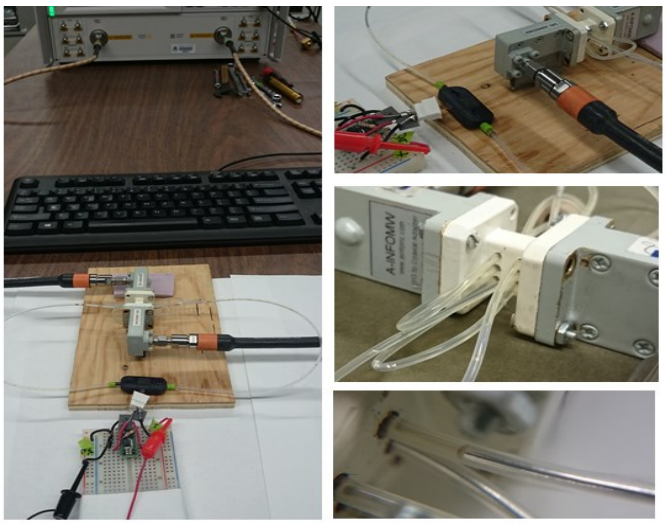

Fig. A-3 The implemented prototype of the microfluidic waveguide switch

A.2 RF Performance

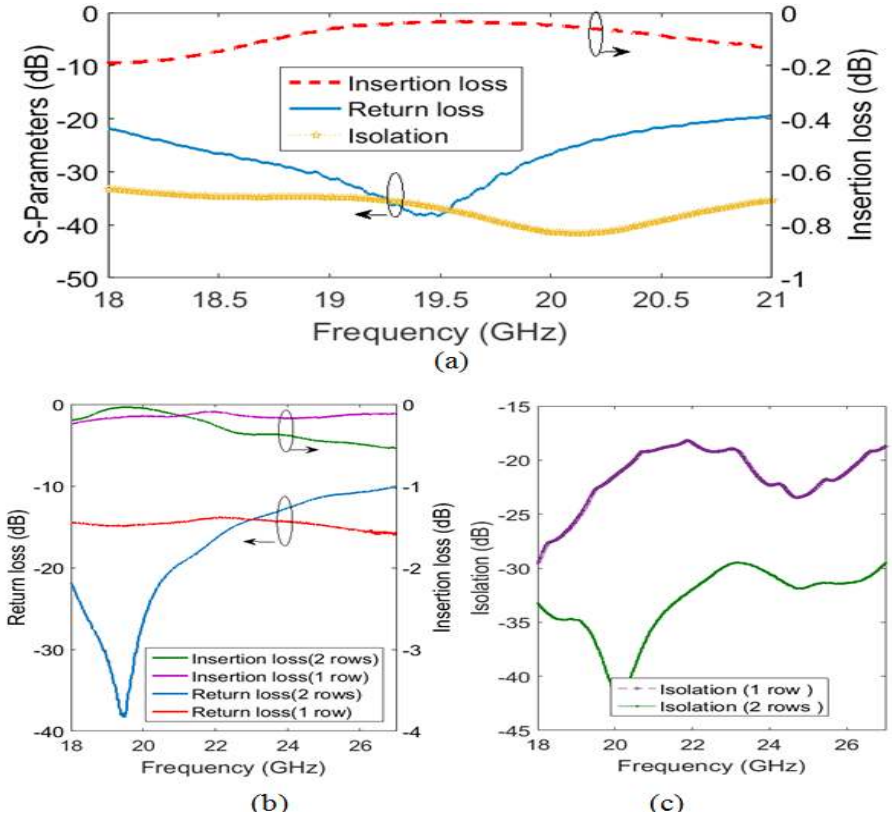

Fig. A-4 The measured RF performance of the proposed microfluidic switch, (a) Narrowband 2-rows, (b) ON State wideband, and (c) OFF State wideband

The RF performance of the switch in both ON and OFF States is measured. The switch with 2 rows of tubes show good matching in a narrow band around 20 GHz presenting 0.1 dB of insertion loss and 20 dB of return loss as shown in Fig. A-4 (a). The isolation is also measured to be better than 30 dB. Wideband performance of the switch for the entire K-band is also measured and presented in Fig. A-4 (b) and Fig. A-4 (c). An insertion loss of less than 0.2 dB and 0.45 dB are achieved for 1-row and 2-rows respectively in the entire K-band (18 GHz-26 GHz), which agrees well with the simulations. The isolation of the switch in the OFF State achieved is better than 17 dB and 30 dB for 1-row and 2-rows respectively.

Appendix B

Extraction of Propagation Constant: Multiline Extraction Technique

A multiline method was used for determining the propagation constants, presented in 3.2.2, from scattering parameter measurements of two transmission line [85][86]. Two lengths of lines were used for the computation using a de-embedding technique. In order to mathematically manipulate the matrixes of the transitions, the S-parameters are converted to the transmission matrix (T-Matrix) which can be cascaded using standard matrix algebra.

The T-parameters are be related to S-parameters as follows.

S-Parameters:
$$\begin{bmatrix} b_1 \\ b_2 \end{bmatrix} = \begin{bmatrix} S_{11} & S_{12} \\ S_{21} & S_{22} \end{bmatrix} \begin{bmatrix} a_1 \\ a_2 \end{bmatrix} \quad \text{(B-1)}$$

T-Parameters:
$$\begin{bmatrix} b_1 \\ a_1 \end{bmatrix} = \begin{bmatrix} T_{11} & T_{12} \\ T_{21} & T_{22} \end{bmatrix} \begin{bmatrix} a_2 \\ b_1 \end{bmatrix} \quad \text{(B-2)}$$

$$\begin{pmatrix} T_{11} & T_{12} \\ T_{21} & T_{22} \end{pmatrix} = \frac{1}{S_{21}} \begin{pmatrix} S_{12}S_{21} - S_{11}S_{22} & S_{11} \\ -S_{22} & 1 \end{pmatrix} \quad \text{(B-3)}$$

The steps taken, for the computation of propagation constant from measured lengths of transmission lines, are adapted directly from [95], and are demonstrated below:

"Since a back-to-back structure can be broken down into three cascaded networks of the input transition, the main transmission line and the output transition, the T-parameters of these three structures can be multiplied in a sequence.

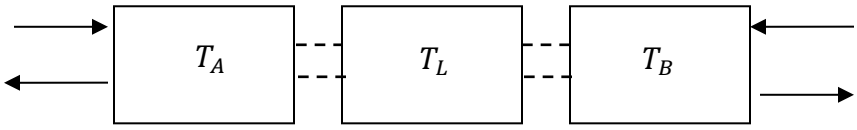

Fig. B-1 The cascaded T-parameters of back-to-back structure

$$T_{DUT} = T_A T_L T_B \quad \text{(B-4)}$$

To extract the T-parameters of the transmission line, the S-parameters of a Thru structure and a Line structure are measured. Using these two measurements, the T-parameters of the transmission line can be calculated using the following steps:

1. The S-parameters of a Thru is measured first and converted to T-parameters.

$$S_{AB} \rightarrow T_{AB} = T_A T_B \tag{B-5}$$

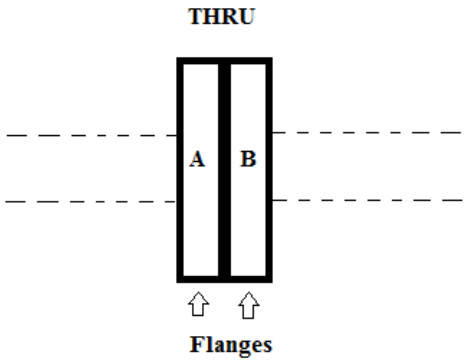

Fig. B-2 THRU

2. The S-parameters of a Line (Thru plus transmission length) is measured and converted to T-parameters.

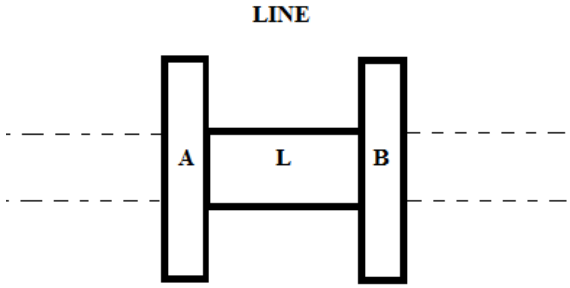

Fig. B-3 LINE

$$S_{ALB} \rightarrow T_{ALB} = T_A T_L T_B \tag{B-6}$$

3. The matrix T is found where T is:

$$\mathrm{T} = \mathrm{T_{ALB}}\mathrm{T_{AB}^{-1}} = \mathrm{T_A}\mathrm{T_L}\mathrm{T_B}\mathrm{T_{AB}^{-1}} = \mathrm{T_A}\mathrm{T_L}\mathrm{T_B}\mathrm{T_B^{-1}}\mathrm{T_A^{-1}} = \mathrm{T_A}\mathrm{T_L}\mathrm{T_A^{-1}} \quad \text{(B-7)}$$

using the cascaded properties of T-parameters.

For the added transmission line, the T-matrix can be written as:

$$\mathrm{T_L} = \begin{bmatrix} \mathrm{e}^{-\gamma \mathrm{L}} & 0 \\ 0 & \mathrm{e}^{\gamma \mathrm{L}} \end{bmatrix} \quad \text{(B-8)}$$

And using (C-8)

$$\mathrm{TT_A} = \mathrm{T_A}\mathrm{T_L} \quad \text{(B-9)}$$

$$\begin{bmatrix} T_1 & T_2 \\ T_3 & T_4 \end{bmatrix}\begin{bmatrix} T_{A1} & T_{A2} \\ T_{A3} & T_{A4} \end{bmatrix} = \begin{bmatrix} T_{A1} & T_{A2} \\ T_{A3} & T_{A4} \end{bmatrix}\begin{bmatrix} e^{-\gamma L} & 0 \\ 0 & e^{\gamma L} \end{bmatrix}$$

Performing the multiplications, we found:

$$T_1.T_{A1} + T_2.T_{A3} = T_{A1}.\,e^{-\gamma L} \quad \text{(B-10)}$$

$$T_3.T_{A1} + T_4.T_{A3} = T_{A3}.\,e^{-\gamma L} \quad \text{(B-11)}$$

$$T_1.T_{A2} + T_2.T_{A4} = T_{A2}.\,e^{\gamma L} \quad \text{(B-12)}$$

$$T_3.T_{A2} + T_4.T_{A4} = T_{A4}.\,e^{\gamma L} \quad \text{(B-13)}$$

From (B-11) and (B-12) we have:

$$\frac{T_{A1}}{T_{A3}} = \frac{T_2}{e^{-\gamma L} - T_1} = \frac{e^{-\gamma L} - T_4}{T_3} \tag{B-14}$$

$$e^{-2\gamma L} - e^{-\gamma L}(T_1 + T_4) + (T_1 T_4 - T_2 T_3) = 0 \tag{B-15}$$

Similarly, from (B-10) and (B-11)

$$e^{2\gamma L} - e^{\gamma L}(T_1 + T_4) + (T_1 T_4 - T_2 T_3) = 0 \tag{B-16}$$

Thus the solution for $e^{-\gamma L}$ and $e^{\gamma L}$ can be found by solving the equations below.

$$G^2 - G(T_1 + T_4) + (T_1 T_4 - T_2 T_3) = 0 \tag{B-17}$$

$$G = K_1.[1 + K_2^{1/2}] \tag{B-18}$$

Where $K_1 = \frac{(T_1 + T_4)}{2}$, $K_2 = 1 - \frac{K_3}{K_1^2}$, and $K_3 = T_1 T_4 - T_2 T_3$

By finding the solution for $e^{-\gamma L} = e^{-(\alpha + j\beta)L}$, the line parameters α and β can be found."